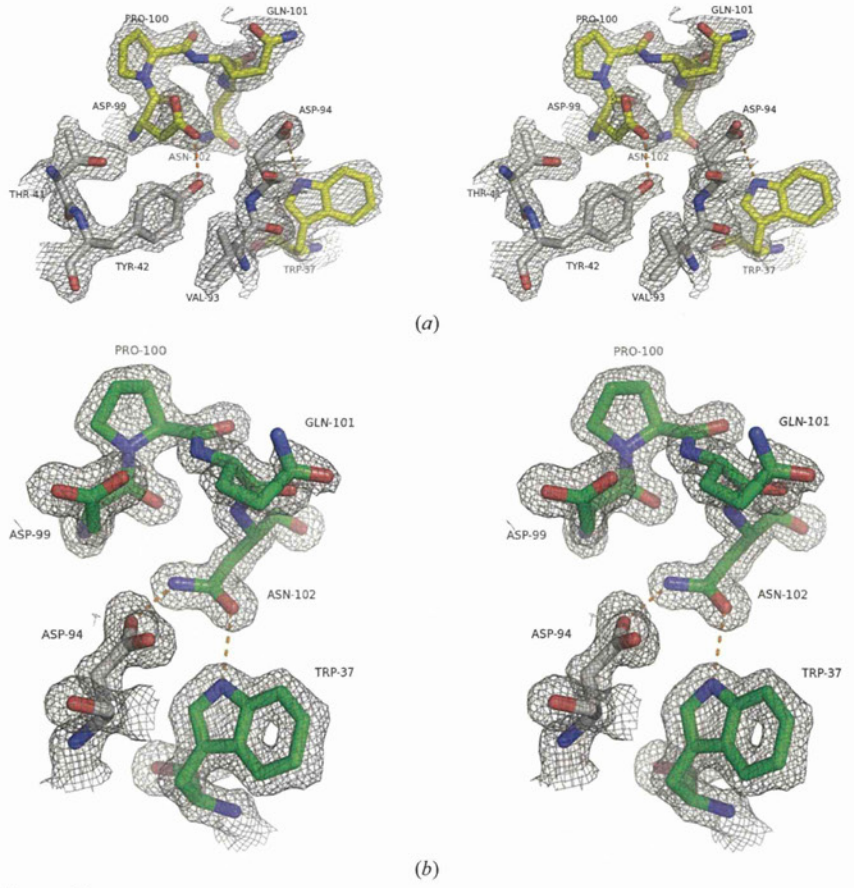

Figure 2
(*a*) A stereoview of the $\alpha_1\beta/\delta_2$ interface of deoxy woolly mammoth Hb showing the $2mF_o - DF_c$ electron-density map at a contour level of 1σ. The structure is shown as a stick model coloured by atom type: oxygen, red; nitrogen, blue. C atoms of the α subunit are coloured white and C atoms of the β/δ subunit are coloured yellow. Hydrogen bonds used as markers of the T state are shown as orange dotted lines. Glnβ/δ101, the principal mutation in mammoth Hb, can be seen at the top of the figure. Figures were produced using *PyMOL* (DeLano, 2002). (*b*) A stereoview of the $\alpha_1\beta/\delta_2$ interface of carbonmonoxy woolly mammoth Hb showing the $2mF_o - DF_c$ electron-density map at a contour level of 1σ. C atoms of the α subunit are coloured white and C atoms of the β/δ subunit are coloured green. Hydrogen bonds used as markers of the R state are shown as orange dotted lines.

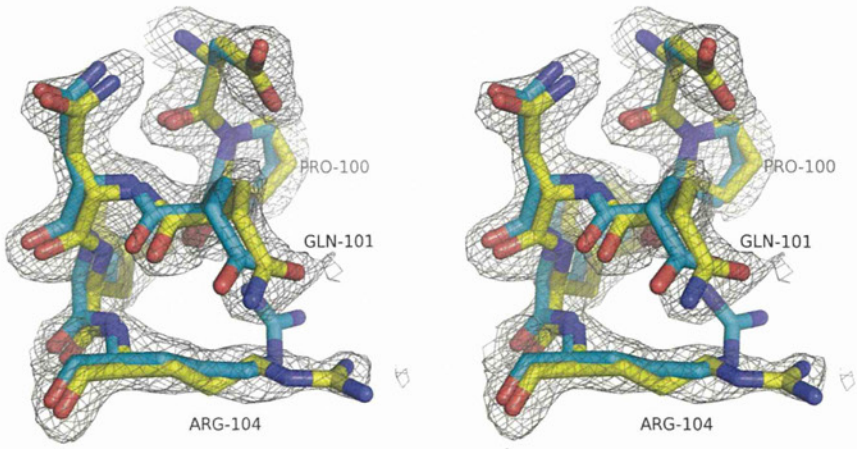

Figure 3
A stereoview showing the overlap of deoxy woolly mammoth Hb and deoxy HbA around Glnβ/δ101. C atoms of the human protein are coloured cyan and the $2mF_o - DF_c$ electron-density map is shown at a contour level of 1σ. Argβ/δ104 adopts a more extended conformation in mammoth Hb, pointing towards its symmetry mate on the opposite side of the central cavity.

3.2. Quaternary structure

There has been considerable debate concerning the nature of the liganded state of Hb (Tame, 1999). Early data from the Perutz group suggested that haem ligands or oxidation to the aquo-met (Fe^{3+}) state drive the protein into the R conformation. Arnone and coworkers later found that liganded HbA can crystallize in a different form called 'R2' (Silva *et al.*, 1992). It was subsequently suggested that the R structure is in fact an artifact of the crystallization conditions and that the R2 structure more accurately reflects the solution structure of the molecule (Srinivasan & Rose, 1994). Unfortunately, minor errors such as a peptide flip and incorrect side-chain rotamers in the highly cited 1983 crystal structure of oxy-HbA (Shaanan, 1983) have been taken as hallmarks of the R state by some authors (Srinivasan & Rose, 1994; Safo & Abraham, 2005), and the lack of a consistent definition of the quaternary conformations has greatly confused the literature. We use the pattern of hydrogen bonding to class a model as T or R state, rather than rotation angles or side-chain rotamers; the residues involved in forming these interactions are all well conserved over millions of years of evolution and are readily modelled in the electron-density maps. Such a definition allows significant conformational variation within both the T and the R states. A number of slightly different crystal structures of liganded Hb have been published, suggesting that the protein samples a relatively large conformational space. It remains debatable whether some of these forms can usefully be called novel quaternary states, since they are little different from the well known R structure. However, NMR analysis of human oxy-Hb in solution shows that it samples a considerable conformational space and is not well represented by either the R or the R2 form alone (Gong *et al.*, 2006; Lukin *et al.*, 2003). More recently, molecular-dynamics simulations have shown that T-state HbA rapidly relaxes to the R state, but does not sample the R2 state on the timescale of the experiment (Hub *et al.*, 2010). The liganded mammoth Hb structures refined here are closer to the R conformation of HbA than the R2 conformation. Like other animal Hbs (Tame, 1999), mammoth Hb supports the idea that liganded Hb is conformationally flexible but generally maintains the hydrogen-bonding

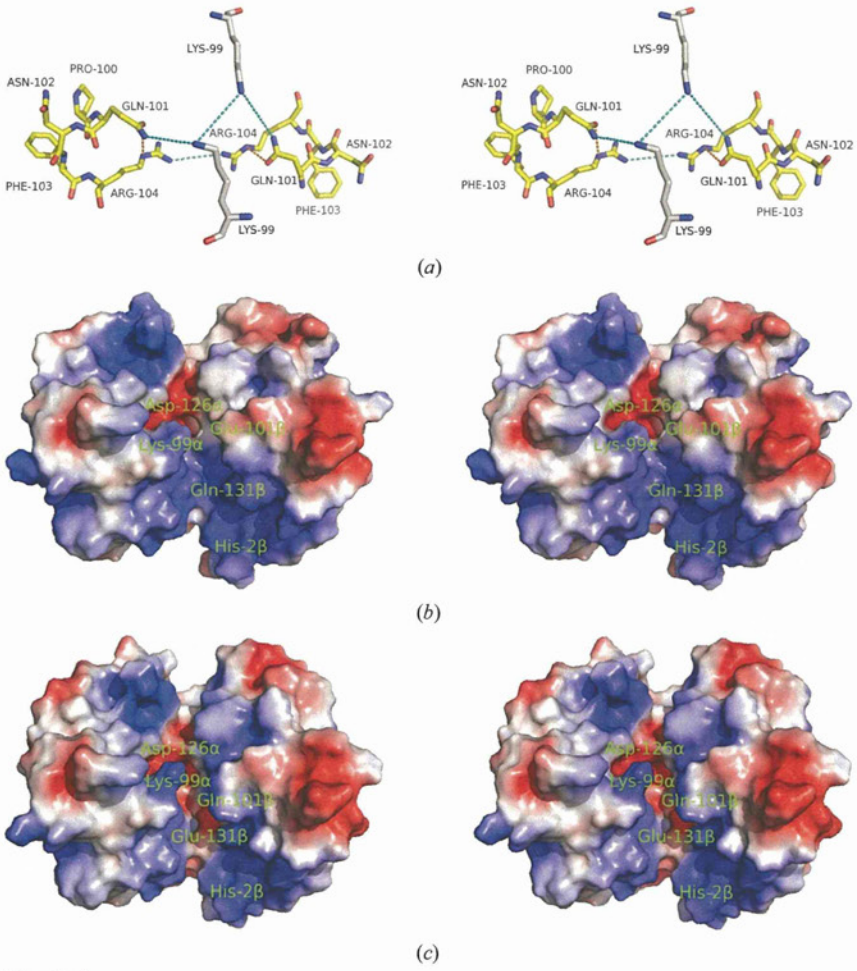

Figure 4
(*a*) A stereoview of the central cavity of deoxy woolly mammoth Hb. C atoms of the α subunit are coloured white and C atoms of the β/δ subunit are coloured yellow. Orange dotted lines indicate distances of between 3 and 4 Å in length and light blue dotted lines indicate distances of between 4 and 7.2 Å in length. In human HbA, the charge on the pairs of lysine and arginine residues is partly countered by Gluβ/δ101. (*b*) A stereoview of the molecular surface of one $\alpha\beta$ dimer of deoxy human HbA coloured by electrostatic potential (red, negative; blue, positive). Colour saturation corresponds to an electron energy of $\pm 3kT$. The α chain is on the left; the central cavity is shown running vertically and the DPG binding site is at the bottom. Aspα126 is responsible for the negatively charged pocket between the two subunits and Lysα99 projects from the α subunit towards Gluβ101. The surface potential was calculated using *APBS* (Baker *et al.*, 2001). (*c*) A similar figure to (*b*) but showing deoxy woolly mammoth Hb. The electrostatic potential is altered from the normal pattern by two mutations: Gluβ/δ101→Gln and Glnβ/δ131→Glu. The potential is essentially unchanged around Asnα131 and Valβ/δ1, which are the sites of chloride binding in other animal Hbs. Lysα99 shows a higher potential in woolly mammoth Hb than in HbA.

pattern shown for the carbonmonoxy and aquo-met models (Table 2).

3.3. Differences between elephant and mammoth Hb

Although the T and R structures of mammoth Hb are highly similar to those of human Hb, several important distinctions are apparent. Histidine residues are important to Hb since they mediate much of the Bohr effect (Busch *et al.*, 1991; Fang *et al.*, 1999; Sun *et al.*, 1997). As in HbA, the C-terminal histidine of the β/δ subunit, Hisβ/δ146(HC3), makes a salt bridge with Aspδ94(FG1) in the T state but not in the R state, so that oxygenation releases protons. Mammoth Hb has 19 histidine residues in the $\alpha\beta$ dimer, two of which, β/δ44(CD3) and β/δ56(DE2), are not present in HbA. Conversely, HbA has Hisβ2(NA2), which is Asn in the mammoth protein, and Hisβ116(G18), which is Arg in the mammoth protein. The histidine residues all have very similar interactions in common except for Hisα50(CE8). This imidazole side chain makes a stable hydrogen bond to Gluα30(B11) of the same subunit in both proteins, but the histidine rotamer is different in one α chain in the asymmetric unit of the deoxy form since Proβ/δ125(H3) in HbA is changed to Asp in mammoth Hb, pulling Hisα30(B11) towards it. However, the interaction between Asp$\beta/\delta_1$125 and His$\alpha_1$50 is unlikely to contribute to the Bohr effect since the histidine maintains a hydrogen bond to Gluα30 in both the T and R states and the second pK_a of the imidazole well above the physiological pH.

The principal feature of interest is how with very modest changes to the protein surface the thermodynamics of oxygen binding may be adapted to an Arctic environment. In the case of mammoth Hb, the enthalpy change of oxygen binding seems to be partly reduced compared with ancestral Hbs through changes in the chloride effect (Campbell *et al.*, 2010). Many vertebrate Hbs, including human Hb, show reduced oxygen affinity in the presence of chloride ions, although high concentrations of chloride, typically 100 m*M*, are required to observe this effect fully. Since chloride binding is very weak, minor changes to the protein may influence it appreciably. The mutation in mammoth Hb at the highly conserved residue Gluβ/δ101(G3) is therefore highly surprising. In HbA, this glutamate residue lies close to Argβ104(G6) (Fig. 3), towards which it is pushed by the perfectly conserved Asp$\alpha_2$94(G1) and Asp$\beta_1$99(G1). The arginine side chain shows different conformations in different T-state structures so that it may form, for example, a hydrogen bond to the carboxyl O atom of Proβ100(G2), but it generally prefers to bind to the side chain of Asnβ139(H17) (Park *et al.*, 2006; Tame & Vallone, 2000). In the deoxy mammoth Hb, Glnβ/δ101(G3) exerts no electrostatic pull on the arginine, allowing it to stretch across the central cavity of the tetramer towards its symmetry mate. The two copies of Argβ/δ104(G6) approach within 5 Å of each other in the T state, whereas in the R-state structure the closest approach of these symmetry-

related arginine residues is almost 6.5 Å. This mutation is therefore expected to destabilize the T state relative to the R state, which is consistent with the elevated intrinsic oxygen affinity of the protein.

The Gluβ101 residue of human Hb adopts a very similar position to that of Glnβ/δ101 in mammoth Hb, so the effects of this mutation appear to arise from electrostatic changes and their influence on nearby residues. It can be seen from Fig. 4 that Glnβ/δ101 lies between Lysα99(G6) and Argβ/δ104(G6), both of which are highly conserved among vertebrates. The mammoth Gluβ/δ101→Gln mutation therefore leads to an increased and concentrated positive charge within the central cavity, which may well draw chloride ions into the protein and increase its sensitivity to this allosteric effector. Mammoth Hb has a significantly higher oxygen affinity than elephant Hb in the absence of heterotropic effectors, but a comparable affinity in the presence of chloride and DPG (Yuan *et al.*, 2011; Campbell *et al.*, 2010), so it appears that repulsion between Lysα99(G6) and Argβ/δ104(G6) (and their symmetry mates) is alleviated by these counterions. Exactly the same behaviour has been reported for Hb Rush by Shih *et al.* (1985), who noted that under stripped conditions the affinity for the first oxygen ligand K_1 is increased but K_4 is unchanged; however, the increased positive charge within the central cavity increases proton-linked chloride binding and restores oxygen affinity to normal in the presence of 100 m*M* chloride. This extra chloride binding reduces the heat of oxygenation exactly as found for mammoth Hb. No site for the extra proton binding has been identified previously, but the structure of mammoth Hb shows that Lysα99(G6) adopts the same position as in human HbA and this residue appears to be the most plausible candidate.

The residue Alaβ/δ12(A9) lies on the surface of mammoth Hb within helix A, close to two lysine residues: Lysβ/δ8(A5) and Lysβ/δ76(E20) (Fig. 5*a*). The C^{α} trace of mammoth Hb is very close to that of human HbA around the N-terminus of the non-α subunit, but is slightly different from that of bovine Hb. Human β globin (like elephant β/δ globin) has a threonine at position 12, but an alanine at position 76. The lysine residues are shared by bovine Hb and have been strongly implicated in chloride ion binding to this protein (Fronticelli, 1990). In bovine Hb, however, main-chain shifts around the N-terminus push Lysβ8(A5) towards Thrβ12(A9) so that the lysine carbonyl O atom makes hydrogen bonds to both the threonine side chain and N atom. Other Hbs only have the main-chain interaction within the A helix. The loss of the threonine at position β/δ12 may have the effect of removing this chloride ion-binding site, although such binding may in any case require the small shift of the A helix found in bovine Hb. We have previously suggested (Campbell *et al.*, 2010) that the mammoth Thrβ/δ12→Ala mutation may allow the Lysβ/δ8 side chain to interact more strongly with the carboxyl group of Aspβ/δ79 on the same subunit and weaken the repulsion of anions around the DPG binding site. Some evidence for such an effect can be seen in one $\alpha\beta$ dimer in the deoxy mammoth Hb model (Fig. 5*b*) but not the other. Even where Lysβ/δ8 does approach Aspβ/δ79(EF3), the hydrogen bond is almost 3.5 Å in length. Although the crystal structures do not suggest any gain or loss of function arising from the Thrβ/δ12→Ala mutation, some effect may occur in the presence of DPG. Finally, the replacement of Alaβ/δ86(F2) by Ser in mammoth Hb is unusual but this surface residue apparently forms no important interactions and the structure gives no suggestion that the functional properties of the protein would be altered in any way. To our knowledge, this region of the protein has not been implicated in chloride or DPG binding in any vertebrate Hb.

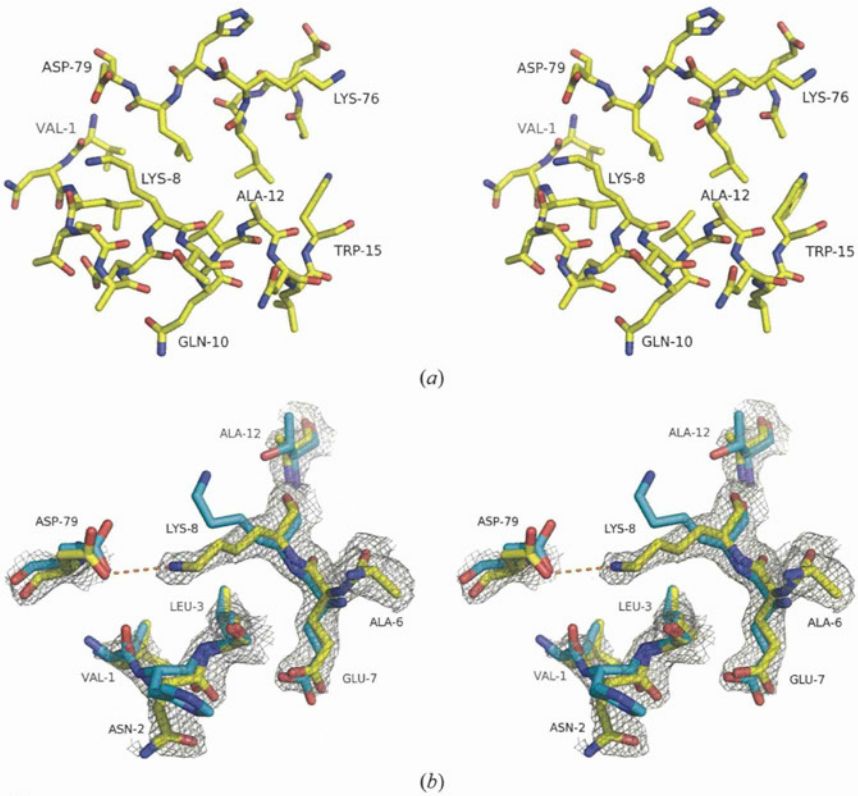

Figure 5
(*a*) The surface of the β/δ subunit of deoxy woolly mammoth Hb, showing the proposed chloride ion-binding site of bovine Hb (Fronticelli *et al.*, 1995). In the subunit shown, Lys8 makes no interaction with Asp79 of the same subunit. (*b*) Stereoview of the deoxy woolly mammoth Hb β/δ subunit not shown in (*a*), with the $2mF_o - DF_c$ map superposed at a level of 1σ. In this case Lysβ/δ8 forms a salt bridge with Aspβ/δ79. Superimposed on this model is deoxy HbA (C atoms coloured cyan). In HbA Lysβ8 can hydrogen bond to Thrβ12.

4. Discussion

The chloride effect of HbA was originally explained, like the DPG effect, by preferential binding to the low-affinity T state changing the allosteric equilibrium of the protein. It was realised early on that the

oxygen affinity of R-state Hb is dependent on the solution conditions, but this effect was largely neglected until the global allostery model was put forward by Yonetani and coworkers (Tsuneshige *et al.*, 2002; Yonetani & Tsuneshige, 2003). Unlike DPG, which can be visualized in crystallographic electron-density maps (Arnone, 1972), chloride proved more difficult to detect in the case of bovine Hb. This led Perutz and coworkers to propose a 'new' type of allosteric effect in which chloride ions simply acted to weaken the repulsion of positively charged groups within the central cavity of the protein (Perutz *et al.*, 1993); since these charges move closer together in the T state than the R state, chloride ions were proposed to stabilize the T state. It was found that even bromide ions could not be detected in the crystal structure of bovine Hb, which was interpreted as demonstrating that there are no fixed binding sites for chloride or bromide within the T-state structure of bovine or human Hb. This view has remained controversial, not least because of the negative nature of the evidence. Considerable experimental work has been carried out on the chloride effect of bovine Hb (Fronticelli, 1990). Like human Hb, bovine Hb loses about 2.2 chloride ions on oxygenation near neutral pH in the presence of 100 m*M* chloride (Perutz *et al.*, 1994; Fronticelli *et al.*, 1995). Mutagenic experiments have implicated the lysine residues at positions β8 and β76 on the outer surface of bovine Hb in chloride binding (Fronticelli *et al.*, 1995), implying a very different mechanism to that of Perutz. As mentioned above, HbA has alanine at position β76, suggesting that the chloride effect may occur through quite different residues in different Hbs. Some data indicate that chloride ions can interact with other Hbs at specific sites. For example, the frog *Telmatobius* lives high in the Andes around Lake Titicaca and its unusually high oxygen-affinity Hb has been found to be unresponsive to chloride (Weber *et al.*, 2002). Sequence comparisons with normal frog Hbs strongly suggest that chloride binding is lost owing to a single mutation in the α chain, Serα131(H14)$\rightarrow$Ala, within the central cavity. In HbA, this serine lies close to the N-terminus of the β subunit of the opposite $\alpha\beta$ dimer, a site implicated in chloride binding to the T state (O'Donnell *et al.*, 1979). This replacement of one uncharged residue by another smaller one can hardly block chloride binding through steric or electrostatic effects. Serα131(H14) is not preserved in bovine or Asian elephant Hb, being replaced in both cases by asparagine. The chloride effect of elephant Hb is notably low (Yuan *et al.*, 2011), yet the positively charged residues within the central cavity are preserved between bovine and elephant Hbs. This result may possibly be reconciled with the Perutz model by the extra negative charge in mammoth and elephant Hb at residue β/δ139 (see below). Comparing elephant and mammoth Hb, it can be seen that the mammoth protein is more sensitive to chloride, while retaining Asnα131(H14). This residue lies over 20 Å from Glu$\beta/\delta_1$101 and Glu$\beta/\delta_2$101, so chloride binding at the site lost from *Telmatobius* Hb can be ruled out. Furthermore, from the structures of mammoth Hb presented here, it is highly unlikely that the protein surface interacts with chloride ions in the manner suggested for bovine Hb. Additional evidence against these surface sites has recently emerged from a comparative study of mole Hbs (Signore *et al.*, 2012).

We are therefore led to conclude that the functional differences between mammoth Hb and elephant Hb arise primarily from the Glnβ/δ101 mutation, with Thrβ/δ12$\rightarrow$Ala possibly contributing a smaller effect. The strong sequence conservation around the site of the mutation suggests that minor changes such as the additional hydrogen bond between His$\alpha_1$50 and Asp$\beta/\delta_1$125 (noted above) may play a role. The replacement of Hisβ/δ2 by Asn will compensate to some extent for the additional positive charge within the central cavity, but this residue lies at the mouth of the cavity over 20 Å from Glnβ/δ101. Within 12 Å of this residue, HbA has a glutamine at position β131(H9) which is replaced by glutamate in mammoth and elephant. This has the effect of restoring charge balance within the tetramer and probably stabilizes the protein to the Gluβ/δ101$\rightarrow$Gln mutation. [Human Hb carrying the Glnβ101 mutation (Hb Rush) is slightly unstable.] At the same time, this extra negative charge within Asian elephant Hb may explain its weak response to chloride ions. Ancestral (and modern) elephant Hb therefore appears to carry a β/δ131 mutation predisposing it to develop a large chloride effect through a single-residue change at β/δ101, while having almost no chloride effect of its own. The structures of woolly mammoth Hb highlight how poorly we understand the chloride binding of different Hbs and suggest that different animal Hbs have evolved quite different interactions with this fundamental heterotropic effector.

References

Adams, J. G., Winter, W. P., Tausk, K. & Heller, P. (1974). *Blood*, **43**, 261–269.

Arnone, A. (1972). *Nature (London)*, **237**, 146–149.

Baker, N. A., Sept, D., Joseph, S., Holst, M. J. & McCammon, J. A. (2001). *Proc. Natl Acad. Sci. USA*, **98**, 10037–10041.

Baldwin, J. & Chothia, C. (1979). *J. Mol. Biol.* **129**, 175–220.

Bohr, C., Hasselbalch, K. & Krogh, A. (1904). *Skand. Arch. Physiol.* **16**, 401–412.

Busch, M. R., Mace, J. E., Ho, N. T. & Ho, C. (1991). *Biochemistry*, **30**, 1865–1877.

Campbell, K. L., Roberts, J. E., Watson, L. N., Stetefeld, J., Sloan, A. M., Signore, A. V., Howatt, J. W., Tame, J. R. H., Rohland, N., Shen, T. J., Austin, J. J., Hofreiter, M., Ho, C., Weber, R. E. & Cooper, A. (2010). *Nature Genet.* **42**, 536–540.

Chervenak, M. C. & Toone, E. J. (1995). *Biochemistry*, **34**, 5685–5695.

DeLano, W. L. (2002). *PyMOL*. http://www.pymol.org.

Emsley, P., Lohkamp, B., Scott, W. G. & Cowtan, K. (2010). *Acta Cryst.* D**66**, 486–501.

Fang, T.-Y., Zou, M., Simplaceanu, V., Ho, N. T. & Ho, C. (1999). *Biochemistry*, **38**, 13423–13432.

Fronticelli, C. (1990). *Biophys. Chem.* **37**, 141–146.

Fronticelli, C., Sanna, M. T., Perez-Alvarado, G. C., Karavitis, M., Lu, A. L. & Brinigar, W. S. (1995). *J. Biol. Chem.* **270**, 30588–30592.

Fung, L. W. & Ho, C. (1975). *Biochemistry*, **14**, 2526–2535.

Giardina, B., Condò, S. G., Petruzzelli, R., Bardgard, A. & Brix, O. (1990). *Biophys. Chem.* **37**, 281–286.

Gong, Q., Simplaceanu, V., Lukin, J. A., Giovannelli, J. L., Ho, N. T. & Ho, C. (2006). *Biochemistry*, **45**, 5140–5148.

Gouet, P., Courcelle, E., Stuart, D. I. & Métoz, F. (1999). *Bioinformatics*, **15**, 305–308.

Hiebl, I., Weber, R. E., Schneeganss, D. & Braunitzer, G. (1989). *Biol. Chem. Hoppe Seyler*, **370**, 699–706.
Ho, C., Yuan, Y. & Simplaceanu, V. (2011). *Hemoglobin: Recent Developments and Topics*, edited by M. Nagai, pp. 17–36. Kerala: Research Signpost.
Hub, J. S., Kubitzki, M. B. & de Groot, B. L. (2010). *PLoS Comput. Biol.* **6**, e1000774.
Imai, K. (1982). *Allosteric Effects in Haemoglobin*. Cambridge University Press.
Jessen, T. H., Weber, R. E., Fermi, G., Tame, J. & Braunitzer, G. (1991). *Proc. Natl Acad. Sci. USA*, **88**, 6519–6522.
Lukin, J. A., Kontaxis, G., Simplaceanu, V., Yuan, Y., Bax, A. & Ho, C. (2003). *Proc. Natl Acad. Sci. USA*, **100**, 517–520.
Monod, J., Wyman, J. & Changeux, J. P. (1965). *J. Mol. Biol.* **12**, 88–118.
Murshudov, G. N., Skubák, P., Lebedev, A. A., Pannu, N. S., Steiner, R. A., Nicholls, R. A., Winn, M. D., Long, F. & Vagin, A. A. (2011). *Acta Cryst.* D**67**, 355–367.
O'Donnell, S., Mandaro, R., Schuster, T. M. & Arnone, A. (1979). *J. Biol. Chem.* **254**, 12204–12208.
Opazo, J. C., Sloan, A. M., Campbell, K. L. & Storz, J. F. (2009). *Mol. Biol. Evol.* **26**, 1469–1478.
Otwinowski, Z. & Minor, W. (1997). *Methods Enzymol.* **276**, 307–326
Park, S.-Y., Yokoyama, T., Shibayama, N., Shiro, Y. & Tame, J. R. H. (2006). *J. Mol. Biol.* **360**, 690–701.
Perutz, M. F. (1970). *Nature (London)*, **228**, 726–739.
Perutz, M. F. (1972). *Nature (London)*, **237**, 495–499.
Perutz, M. F. (1983). *Mol. Biol. Evol.* **1**, 1–28.
Perutz, M. F., Fermi, G., Poyart, C., Pagnier, J. & Kister, J. (1993). *J. Mol. Biol.* **233**, 536–545.
Perutz, M. F. & Imai, K. (1980). *J. Mol. Biol.* **136**, 183–191.
Perutz, M. F., Shih, D. T. & Williamson, D. (1994). *J. Mol. Biol.* **239**, 555–560.
Perutz, M. F., Wilkinson, A. J., Paoli, M. & Dodson, G. G. (1998). *Annu. Rev. Biophys. Biomol. Struct.* **27**, 1–34.
Razynska, A., Fronticelli, C., Di Cera, E., Gryczynski, Z. & Bucci, E. (1990). *Biophys. Chem.* **38**, 111–115.
Safo, M. K. & Abraham, D. J. (2001). *Protein Sci.* **10**, 1091–1099.
Safo, M. K. & Abraham, D. J. (2005). *Biochemistry*, **44**, 8347–8359.
Schay, G., Smeller, L., Tsuneshige, A., Yonetani, T. & Fidy, J. (2006). *J. Biol. Chem.* **281**, 25972–25983.
Shaanan, B. (1983). *J. Mol. Biol.* **171**, 31–59.
Shibayama, N., Miura, S., Tame, J. R. H., Yonetani, T. & Park, S.-Y. (2002). *J. Biol. Chem.* **277**, 38791–38796.
Shih, D. T.-B., Jones, R. T., Imai, K. & Tyuma, I. (1985). *J. Biol. Chem.* **260**, 5919–5924.
Signore, A. V., Stetefeld, J., Weber, R. E. & Campbell, K. L. (2012). *J. Exp. Biol.* **215**, 518–525.
Silva, M. M., Rogers, P. H. & Arnone, A. (1992). *J. Biol. Chem.* **267**, 17248–17256.
Srinivasan, R. & Rose, G. D. (1994). *Proc. Natl Acad. Sci. USA*, **91**, 11113–11117.
Sun, D. P., Zou, M., Ho, N. T. & Ho, C. (1997). *Biochemistry*, **36**, 6663–6673.
Tame, J. R. H. (1999). *Trends Biochem. Sci.* **24**, 372–377.
Tame, J. R. H. & Vallone, B. (2000). *Acta Cryst.* D**56**, 805–811.
Tame, J. R. H., Wilson, J. C. & Weber, R. E. (1996). *J. Mol. Biol.* **259**, 749–760.
Tsuneshige, A., Park, S. & Yonetani, T. (2002). *Biophys. Chem.* **98**, 49–63.
Vagin, A. & Teplyakov, A. (2010). *Acta Cryst.* D**66**, 22–25.
Weber, R. E. (2007). *Respir. Physiol. Neurobiol.* **158**, 132–142.
Weber, R. E. & Campbell, K. L. (2011). *Acta Physiol. (Oxf.)*, **202**, 549–562.
Weber, R. E., Ostojic, H., Fago, A., Dewilde, S., Van Hauwaert, M. L., Moens, L. & Monge, C. (2002). *Am. J. Physiol. Regul. Integr. Comp. Physiol.* **283**, R1052–R1060.
Winn, M. D. *et al.* (2011). *Acta Cryst.* D**67**, 235–242.
Yokoyama, T., Chong, K. T., Miyazaki, G., Morimoto, H., Shih, D. T.-B., Unzai, S., Tame, J. R. H. & Park, S.-Y. (2004). *J. Biol. Chem.* **279**, 28632–28640.
Yokoyama, T., Neya, S., Tsuneshige, A., Yonetani, T., Park, S.-Y. & Tame, J. R. H. (2006). *J. Mol. Biol.* **356**, 790–801.
Yonetani, T., Park, S. I., Tsuneshige, A., Imai, K. & Kanaori, K. (2002). *J. Biol. Chem.* **277**, 34508–34520.
Yonetani, T. & Tsuneshige, A. (2003). *C. R. Biol.* **326**, 523–532.
Yuan, Y., Shen, T.-J., Gupta, P., Ho, N. T., Simplaceanu, V., Tam, T. C. S., Hofreiter, M., Cooper, A., Campbell, K. L. & Ho, C. (2011). *Biochemistry*, **50**, 7350–7360.

http://dx.doi.org/10.1016/j.jmb.2012.07.012 J. Mol. Biol. (2012) 423, 351–364

Contents lists available at www.sciencedirect.com

Journal of Molecular Biology

journal homepage: http://ees.elsevier.com.jmb

Crystal Structures of Penicillin-Binding Protein 3 (PBP3) from Methicillin-Resistant *Staphylococcus aureus* in the Apo and Cefotaxime-Bound Forms

Hisashi Yoshida[1], Fumihiro Kawai[1], Eiji Obayashi[1], Satoko Akashi[2], David I. Roper[3], Jeremy R. H. Tame[1]* and Sam-Yong Park[1]*

[1]*Protein Design Laboratory, Yokohama City University, Suehiro 1-7-29, Tsurumi-ku, Yokohama 230–0045, Japan*
[2]*Structural Biology Laboratory, Yokohama City University, Suehiro 1-7-29, Tsurumi-ku, Yokohama 230–0045, Japan*
[3]*School of Life Sciences, University of Warwick, Gibbet Hill Road, Coventry CV4 7AL, UK*

Received 30 April 2012;
received in revised form
4 July 2012;
accepted 16 July 2012
Available online
27 July 2012

Edited by R. Huber

Keywords:
antibiotic;
MRSA;
protein complex;
analytical ultracentrifugation;
mass spectrometry

Staphylococcus aureus is a widespread Gram-positive opportunistic pathogen, and a methicillin-resistant form (MRSA) is particularly difficult to treat clinically. We have solved two crystal structures of penicillin-binding protein (PBP) 3 (PBP3) from MRSA, the apo form and a complex with the β-lactam antibiotic cefotaxime, and used electrospray mass spectrometry to measure its sensitivity to a variety of penicillin derivatives. PBP3 is a class B PBP, possessing an N-terminal non-penicillin-binding domain, sometimes called a dimerization domain, and a C-terminal transpeptidase domain. The model shows a different orientation of its two domains compared to earlier models of other class B PBPs and a novel, larger N-domain. Consistent with the nomenclature of "dimerization domain", the N-terminal region forms an apparently tight interaction with a neighboring molecule related by a 2-fold symmetry axis in the crystal structure. This dimer form is predicted to be highly stable in solution by the PISA server, but mass spectrometry and analytical ultracentrifugation provide unequivocal evidence that the protein is a monomer in solution.

Introduction

Peptidoglycan is the principal component of the bacterial cell wall synthesized by penicillin-binding proteins (PBPs).[1,2] In the case of the Gram-positive *Staphylococcus aureus*, it forms a layer approximately 30 nm thick around the cell. *S. aureus* commonly colonizes human skin and upper respiratory tract, especially the nasal passages, but may cause serious infections under certain circumstances, such as injury or surgery. A wide variety of clinical conditions are due to *S. aureus* infection, which may also produce toxic shock syndrome. Strains resistant to benzylpenicillin arose in the 1950s but were successfully treated with methicillin, a simple derivative of benzylpenicillin carrying two extra methoxy groups that rendered the drug less readily degradable by β-lactamases. MRSA (*m*ethicillin-*r*esistant *S. aureus*) initially arose due to the acquisition of the *mecA* gene that encodes PBP2a,[3] and now multi-resistant MRSA presents a very significant clinical challenge.[4] Methicillin resistance may alternatively be due to the secretion of β-lactamases.[5] Since peptidoglycan is

**Corresponding authors.* E-mail addresses:
jtame@tsurumi.yokohama-cu.ac.jp;
park@tsurumi.yokohama-cu.ac.jp.

Present addresses: F. Kawai, Department of Biology and Biochemistry, University of Houston, Houston, TX 77204, USA; E. Obayashi, Department of Biochemistry, Shimane University School of Medicine, Izumo 693–8501, Japan.

Abbreviations used: PBP, penicillin-binding protein; Se-Met, selenomethionine; TEV, tobacco etch virus; nanoESI, nanoelectrospray ionization; PDB, Protein Data Bank.

almost invariably required for bacterial viability and absent from eukaryotes, PBPs remain attractive drug targets. In both Gram-positive and Gram-negative bacteria, the stem peptide of the peptidoglycan precursor ends with two D-alanine residues, the last of which is released in the transpeptidation reaction. β-Lactam antibiotics are suicide substrates that mimic this dipeptide,[6] forming a covalent adduct with PBPs that blocks further transpeptidase or carboxypeptidase activity.

The transpeptidation active sites of all PBPs studied to date have several strictly conserved motifs. The active-site serine residue is found at the start of helix α2 (by the standard naming convention), three residues before a conserved lysine, to make an SxxK motif. A second motif, SxN, is found on a loop between helices α4 and α5, and a KTG motif is located very close to the active site on strand β3. Resistance to β-lactams may arise through a variety of mechanisms, such as the expression of hydrolases that rapidly destroy the drug. Intrinsic resistance may also develop within the PBPs themselves, lowering their affinity for substrates sufficiently to function in the presence of antibiotics. These mutations may operate through rather indirect mechanisms, such as altered protein flexibility, which are not immediately apparent from simple visual inspection of protein models.[7]

PBPs are classed in two major groups by size.[8] Low-molecular-weight PBPs are single-domain proteins that principally function as DD-carboxypeptidases to restrict the level of cross-linking; they are often nonessential.[9] HMW PBPs (*h*igh-*m*olecular-*w*eight *PBPs*) carry several domains, only one of which acts on peptidoglycan peptides. Class A HMW PBPs also possess the essential transglycosylation activity, whereas the extra domain of class B HMW PBPs has unknown function. *S. aureus* has four PBPs (PBP1–PBP4), of which only PBP4 is a low-molecular-weight PBP. It has been implicated in the drug resistance of community-acquired MRSA,[10] and its crystal structure has been determined.[11] PBP3 (encoded by the *pbpC* gene) has a C-terminal penicillin-binding domain, and its N-terminal domain is well conserved when compared to other species, so that *S. aureus* PBP3 is found almost unaltered in several species of *Bacillus* (such as *Bacillus cereus* and *Bacillus anthracis*) and has 44% identity with PBP2a of *Bacillus subtilis*.[12] Note that the numbering of PBPs arose historically from migration by SDS-PAGE and, therefore, may not reflect sequence similarity across species—PBP3 of *S. aureus* is similar to PBP2 of *Escherichia coli*, and PBP3 of *E. coli* is similar to PBP1 of *S. aureus*. PBP3 of *E. coli* is part of the divisome and required for construction of the septum prior to cell division; it is associated with the flippase FtsW[13] and other enzymes with roles in cell wall synthesis.[14,15] PBP3 of *S. aureus* was reported to be involved in cell division and essential,[16] but later work with a deletion mutant showed that it is not required for cell survival.[12] The deletion mutant showed normal growth with no antibiotics present but severe shape abnormalities and septation defects under sublethal concentrations of methicillin, suggesting that PBP1 and PBP2 may functionally replace PBP3.[12] PBP3 is more sensitive to methicillin than either PBP1 or PBP2, but loss of PBP3 appears to increase methicillin resistance to some degree.

Crystal structures are known for class A and class B PBPs including *E. coli* (PBP1b[17]), *Neisseria gonorrhoeae* (NG-PBP2[18]), *Pseudomonas aeruginosa* (PA-PBP3[19,20]), *Streptococcus pneumoniae* (SP-PBP1a,[21] SP-PBP2x,[22] and SP-PBP2b[7]), and *S. aureus* (SA-PBP2[23] and SA-PBP2a[24]). In this paper, we report the crystal structure of PBP3 from *S. aureus*, determined using heavy atoms and anomalous scattering, and compare it with previously refined HMW PBP models. We also report the reactivity of SA-PBP3 with a variety of β-lactams, measured using mass spectrometry, and try to relate these to the protein structure.

Results

A plasmid was created to express, in *E. coli*, the portion of the *S. aureus* PBP3 gene expected to encode the structured region of the protein, omitting the N-terminal signal peptide and adjacent hydrophobic residues believed to anchor the protein to the cell membrane. This construct permitted high-level cytoplasmic expression of soluble protein, including the sequence from residue 46 to the C-terminus (residue 691), with a cleavable N-terminal histidine tag. Crystals were grown of the apo form. The crystals diffracted to a maximum resolution of 2.3 Å and contain two copies of the protein in the asymmetric unit. Phasing was attempted by molecular replacement using the known model of PBP3 from *S. pneumoniae* (SP-PBP2b)[7] and *P. aeruginosa* (PA-PBP3),[19] but this failed to give convincing solutions using the entire structure as a search model. Solutions were obtained using the C-terminal β-lactam-binding domain alone, but not the N-domain, and molecular replacement ultimately failed to yield a satisfactory model. Therefore, crystals were prepared with selenomethionine (Se-Met) in place of methionine or with bound heavy atoms to allow experimental phase determination. The protein model was constructed *de novo* without reference to earlier models and was largely built with the automatic tools in the PHENIX suite.[25] Although much of the model is covered by electron density of high quality, several turn regions show notably poorly defined geometry and are apparently highly flexible. No residues are

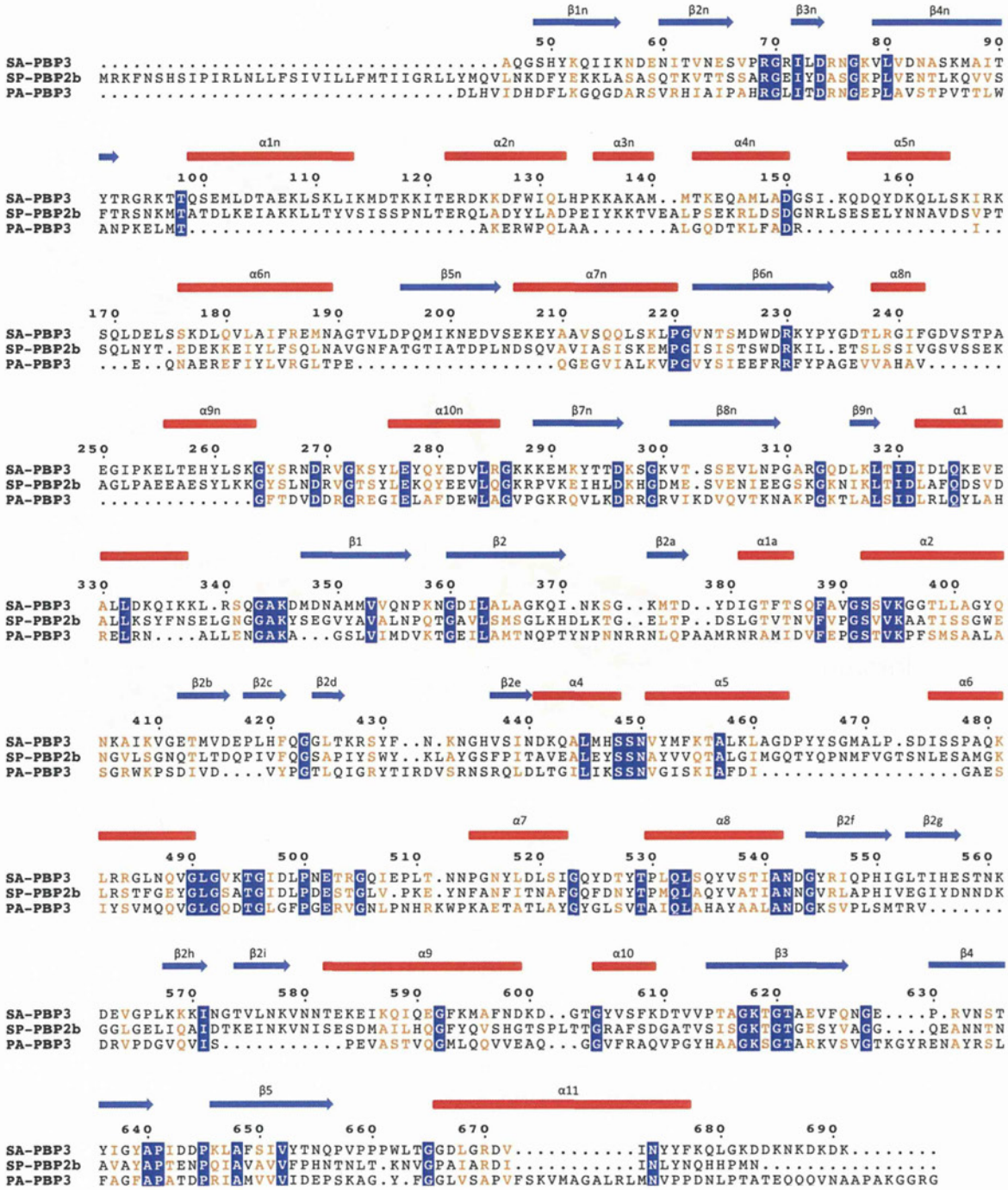

Fig. 1. A sequence and structural alignment of MRSA PBP3 with SP-PBP2b (*S. pneumoniae* R6) and PA-PBP3 (*P. aeruginosa*). α-Helices in the PBP3 model are indicated with red bars, and β-sheets are indicated with blue arrows. Residues common to all three sequences are shown in white on blue. The conserved SxxK, SxN, and KTG motifs at the active site are found at residues 392–395, 448–450, and 618–620, respectively. The active-site serine is Ser392. The figure was made with ESPript.[26]

missing from the model except residues 627–628 (chain A) and 602 (chain B) and at the C-terminus from residue 678 onwards. The secondary structure is shown in Fig. 1.

The crystal structure shows SA-PBP3 to resemble strongly other class B PBPs, having two domains, a C-terminal transpeptidase domain, and an N-terminal nonenzymatic domain. Overall, the two copies

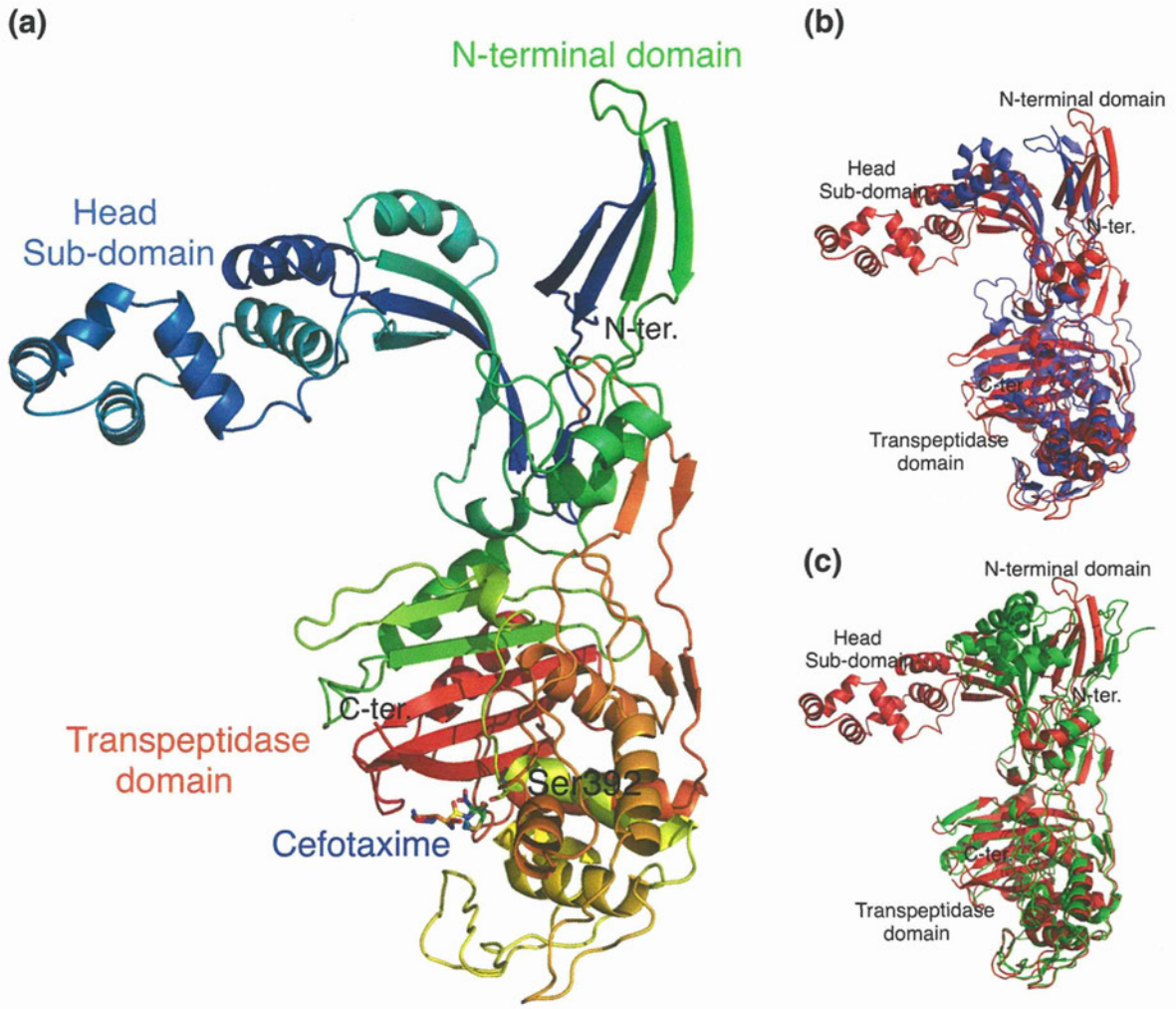

Fig. 2. The overall structure of PBP3. (a) The C^{α} trace of SA-PBP3, colored from blue (N-terminus) to red (C-terminus). The non-catalytic N-terminal domain includes a so-called head sub-domain (residues 77–237). The active site of the transpeptidation domain (Ser392) is shown with covalently bound cefotaxime. (b) Structural overlay of the overall structure of native PBP3 (red) with that of PBP3 of *P. aeruginosa* (blue; PDB ID 3OC2). Structural alignment was carried out automatically with SSM (secondary-structure matching)[30] through Coot. We matched 379 residues of the penicillin-binding domain, with a sequence identity of 22.4% and a final rmsd of 2.3 Å. (c) Overlay of SA-PBP3 (red) with PBP2b from *S. pneumoniae* (green; PDB ID 2WAE). The two models overlap closely with SA-PBP3 over the penicillin-binding domain, but SA-PBP3 shows a considerably larger head domain, with a greater level of similarity to PA-PBP3 than SP-PBP2b. We overlaid 438 residues of the penicillin-binding domain with 38.4% sequence identity and 1.9 Å rmsd.

of the apoprotein in the asymmetric unit have a C^{α} rmsd of 2.6 Å. Non-crystallographic symmetry restraints were not used in the refinement. For the head domain (residues 46–76 and 238–319), the rmsd is 0.99 Å, and for the transpeptidase domain (residues 320–678), the rmsd is 1.3 Å. Comparing the A chains of the native and cefotaxime-bound models, the C^{α} rmsd is 0.39 Å, and for the B chains, the C^{α} rmsd is 0.58 Å, indicating that drug binding to the crystal causes a smaller conformational change than the inherent differences between the copies of the protein in the asymmetric unit. Structural overlays suggest that there is considerable flexibility about the inter-domain hinge of HMW PBPs,[19,27] but the non-penicillin-binding domain of *E. coli* PBP3 is required for correct folding of the protein.[28] In previously determined class B structures, the N-terminal domain includes a so-called "head domain" that is largely α-helical. In PA-PBP3, this contiguous and compact domain extends over residues 80–149,[19] includes four α-helices and three β-strands, and corresponds to the so-called PBP-dimer domain identified by Pfam.[29] It is slightly larger in PBP2b from *S. pneumoniae*[24] but substantially extended in the present SA-PBP3 structure by five extra α-helices extending from Glu122 to Ser175, apparently arising from a single insertion into an ancestral form. Although Pfam

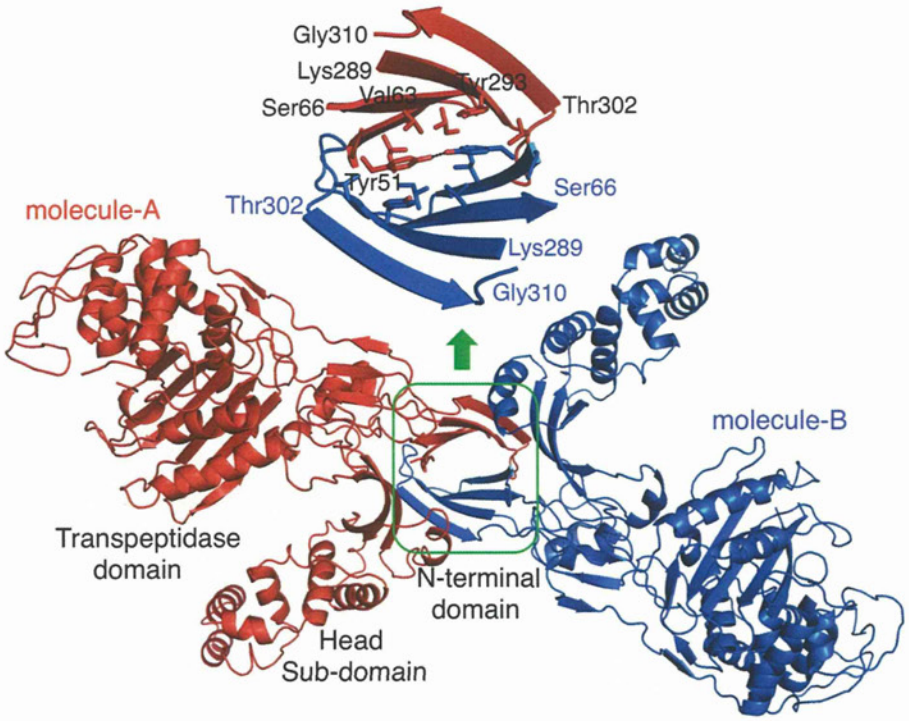

Fig. 3. The principal crystal contact between neighboring molecules. The C^{α} traces of the two molecules are colored red and blue. The self-complementary surface includes Tyr51, which hydrogen bonds to its symmetry equivalent, and also contacts Tyr293 of the opposite chain.

confidently identifies the PBP-dimer domain from the SA-PBP3 sequence, the match is only convincing over residues 179–247, which form widespread structural elements and not a compact domain. The extra C-terminal domain found in PBP2x[22] is not present in SA-PBP3 (Fig. 2).

An interesting feature of the SA-PBP3 structure is the contact formed between the two molecules in the asymmetric unit. Two β-hairpins on each molecule (residues 49–66 and 289–310) associate through non-crystallographic 2-fold symmetry to create a β-sandwich with a total buried surface area of 2730 Å^2 (Fig. 3). This interface is confidently predicted by PISA,[31] leading to stable dimer formation in solution, with a ΔG of dissociation of 6.9 kcal/mol. For comparison, PISA finds no likely oligomeric structure for PA-PBP3, which is believed to be a monomer from gel-filtration results.[19] However, analytical ultracentrifugation shows that the protein exists as a monomer in solution (Fig. 4). To confirm the solution state of the protein, we measured the mass by electrospray mass spectrometry, also indicating the absence of dimers (Fig. 4). Prediction of ligand binding affinity from buried surface areas, hydrogen bond counting, or similar analysis of static crystallographic models is popular but known to be highly unreliable.[32] SA-PBP3 is the first example, to our knowledge, of such a high predicted ΔG from the PISA server proving incorrect. The estimation of separate entropy and enthalpy changes on ligand binding from a static model of a complex, with no regard for experimental conditions, is an exercise in data fitting that is unjustified by thermodynamics.[33] While bioinformatics tools such as Pfam and PISA are without doubt highly useful, their results are not completely reliable and the "PBP-dimer" domain may, in fact, not always self-associate.

Active site

The active-site serine (Ser392) faces a groove running along strand β3 that is approximately 20 Å deep and 15 Å wide, allowing access for peptidoglycan and/or β-lactams (Fig. 5). β3 includes the KS/TG motif (residues 618–621). The SXN motif (residues 448–450) occurs between two helices and the catalytic serine. These three motifs interact through hydrogen bonds; in the apo form, for example, Lys618 hydrogen bonds to Ser448 side chain and the main-chain oxygen of Ser392. The side chain of Ser392 hydrogen bonds to Lys395 and faces away from the other motifs. The active site is open but is more occluded than in *E. coli* PBP4, which is readily inhibited by β-lactams.[34] In the case of SA-PBP2a, which is highly resistant to β-lactams, the active site undergoes significant conformational change on binding an inhibitor, the active-site serine moving up to 1.8 Å away from strand β3.[24] SA-PBP3

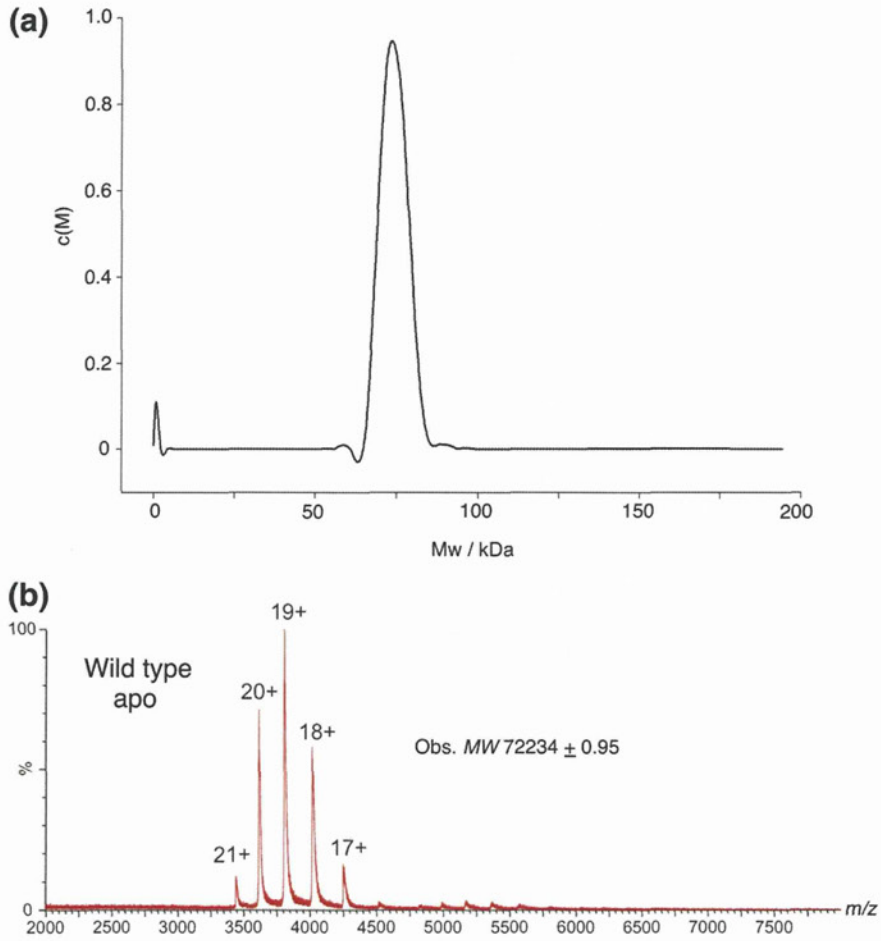

Fig. 4. The solution state of the protein. (a) The association state of the protein in solution was determined by analytical ultracentrifugation. One sharp peak was observed with a sedimentation coefficient of 4.04, consistent with a single species in solution with a molecular mass close to 75 kDa. The expected mass of the monomer is 72,234 Da. No evidence for higher-molecular-weight species was observed, indicating that the protein shows no self-association under the conditions used. (b) NanoESI mass spectrum of native PBP3. Molecular ions with overall charge of 17+ to 21+ were observed in the spectrum, and the molecular mass of PBP3 was calculated to be 72,234.34±0.95, suggesting that PBP3 exists only as a monomer under the experimental conditions in aqueous solution.

shows no such movements, consistent with its relative ease of inhibition,[35] and crystals of the apoenzyme could be soaked directly with substrate. (In the case of the class A enzyme *S. pneumoniae* PBP1b, it was necessary to use an Asn-to-Gly mutant to open up the active site and facilitate inhibitor soaking.[36]) Most of the residues in the immediate vicinity of any bound inhibitor are conserved between PBP2, SA-PBP2a, and SA-PBP3. However, even though Tyr446 of PBP2a interacts with the aromatic ring of bound methicillin,[24] the equivalent residue of PBP3, Tyr430, points away from the active site and sits between Phe341 and His447. It does not appear to play a role in enhancing substrate binding.

Another unique feature of the SA-PBP3 structure is the shortened α11 helix. In NG-PBP2 and SA-PBP2a, the equivalent helix lies near bound β-lactams, potentially sterically hindering access to the active site. Mutations in this region play an important role in antibiotic resistance in NG-PBP2, without causing any substantial change in local structure.[18] In SA-PBP3, this helix is shorter, and residues at its N-terminus form a loop (residues 655–664) that carries apolar residues including the sequence VPPPWL, which extends toward the active site and may influence the approach of hydrophobic substrates. This might suggest a preference of PBP3 for cephalexin, with a simple benzyl side group, to the more polar cefotaxime carrying a free amine on a thiazolidine ring. Cefotaxime, however, appears to be the more effective inhibitor from our results. This observation is not entirely surprising as it is found that disordered regions or effects far from the active site may have a considerable effect on the substrate-

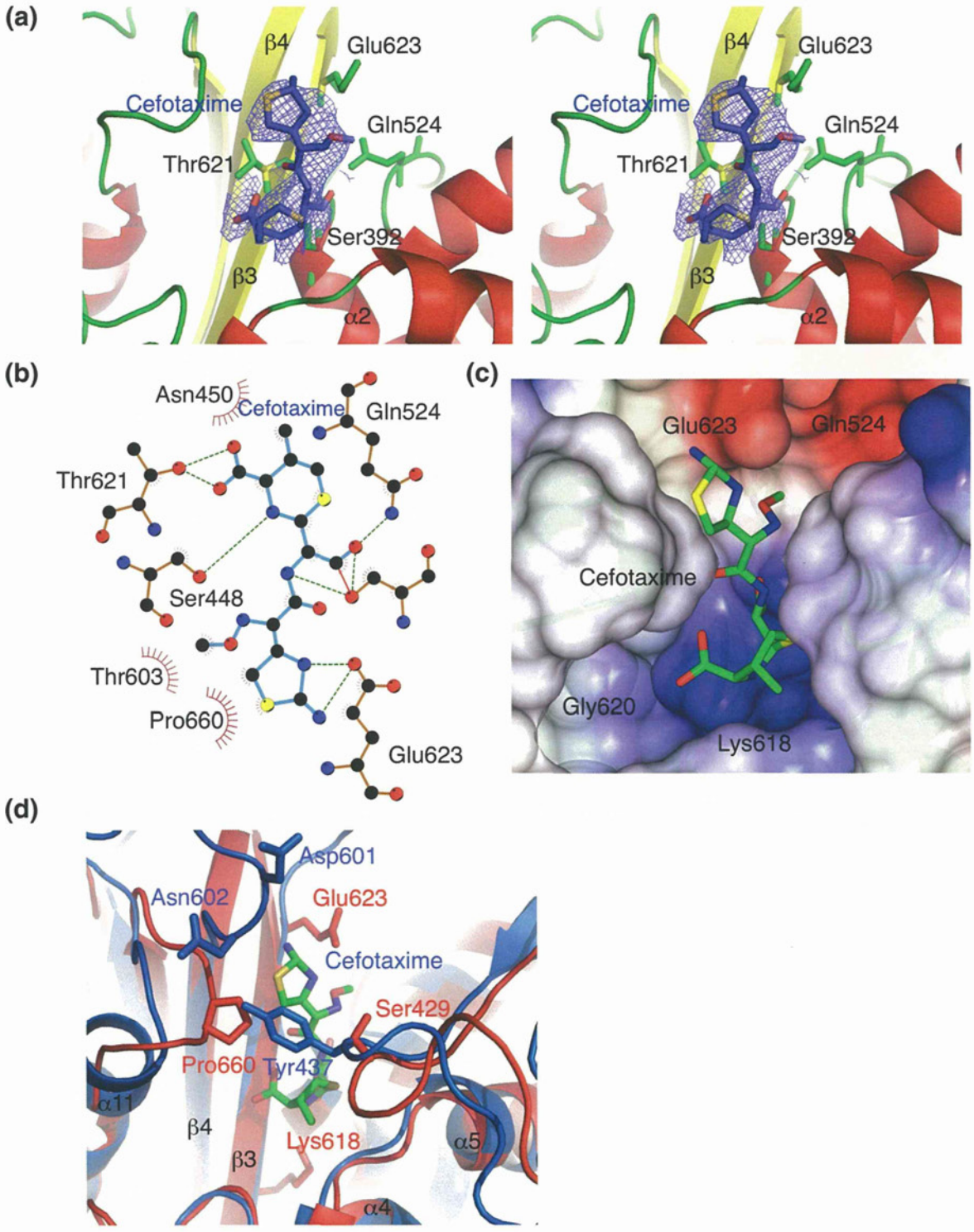

Fig. 5. The interaction of PBP3 with cefotaxime. (a) The 2mFo–DFc electron density omit map, shown in stereo and contoured at a level of 1.1 σ, covering the covalently bound residue of the drug in the active site. (b) Schematic diagram showing the protein–drug interactions. The hydrophobic interactions between cefotaxime and the protein (distance, 3.5–3.9 Å) are indicated with dotted arcs. Hydrogen bonds (2.5–3.4 Å) are shown as green dotted lines. (c) Stick representation of the drug over the molecular surface of the protein. The protein surface is colored by electrostatic potential (blue, positive), showing the charged patches near the active site. Carbon atoms of the drug are colored green; nitrogen, blue; oxygen, red; and sulfur, yellow. (d) Comparison of the active sites of the SA-PBP3 with cefotaxime complex (red) and the PBP2 of *S. aureus* (blue; PDB ID 2OLU). The models were overlapped by SSM. The penicillin-binding site is occluded by Tyr437 in the case of apo PBP2 but remains open in the apo form of SA-PBP3.

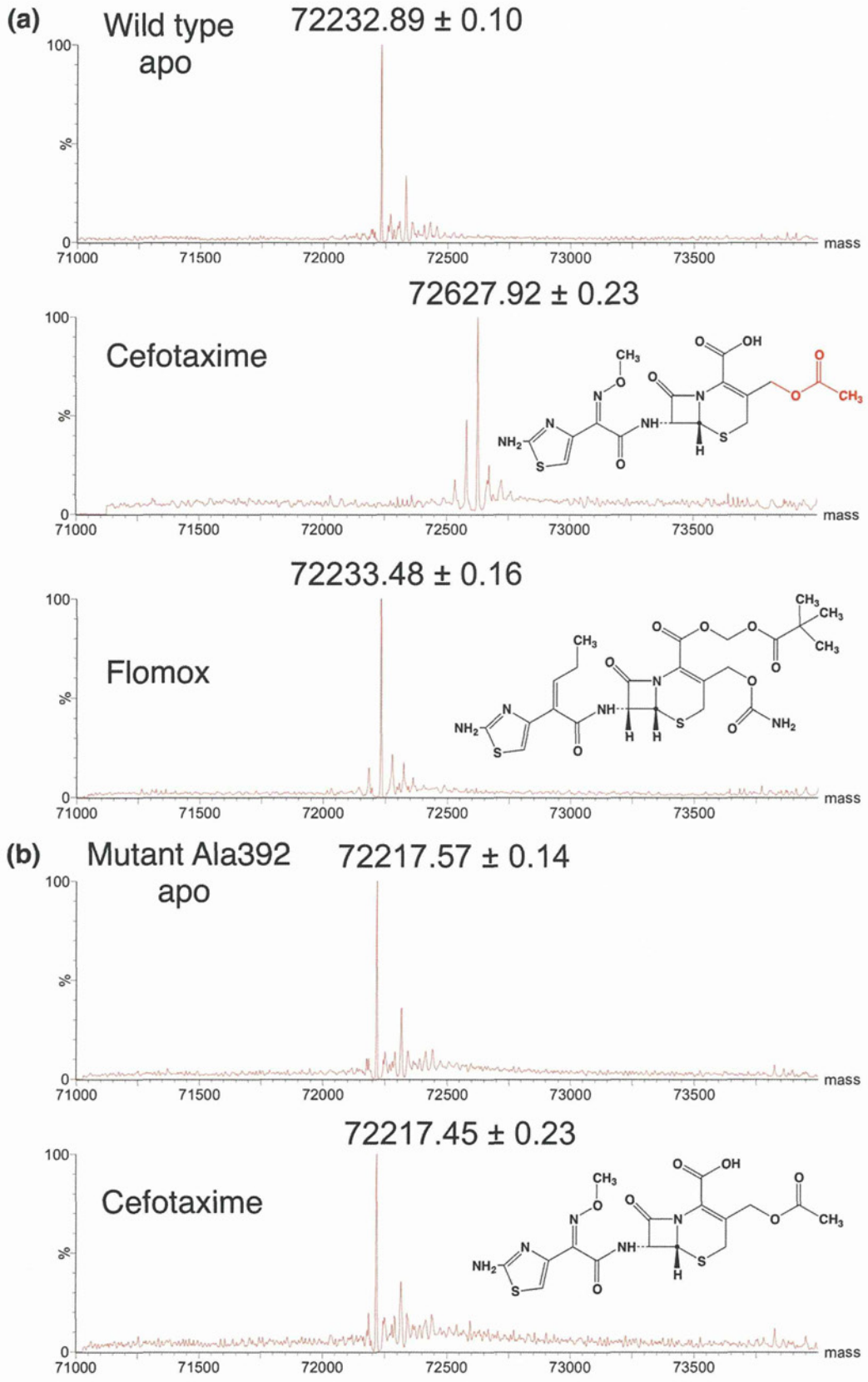

Fig. 6 (*legend on next page*)

binding properties of PBPs, making functional predictions from the structure unreliable.[37]

Cefotaxime-bound structure

Attempts were made to determine the structure of SA-PBP3 with cefotaxime, cephalexin, or ampicillin bound by soaking the apo crystals for 12 h in the presence of these compounds. Refinement proceeded readily from the apo model, but it became clear that the active site is empty in the case of crystals soaked in ampicillin or cephalexin, and therefore, these structures are no different from the apo model (data not shown). Cefotaxime remains covalently bound and clearly visible in the electron density map, although no density is observed for the acetyl group (Fig. 5). Overall, the changes to the structure on binding cefotaxime are very minor, including the conserved catalytic residues. Thr619 (of the KTG motif) and Thr621 rotate away from the drug. The C^{α} atom of Thr621 moves roughly 1 Å. Ser429 of the SXN loop turns away from the bound drug, and Glu623, shortly downstream from the KTG motif, turns slightly toward the solvent. Pro660 shifts about 1.3 Å, together with a slight twist of Trp662. None of these movements appears highly strained, and the active site of the apo form is primed for substrate binding.

Failure to observe antibiotics other than cefotaxime in the SA-PBP3 active site led us to examine the reactivity of the protein by mass spectrometry. The protein was exposed to a variety of compounds and then denatured with acetonitrile before mass measurement. A selection of the results is shown in Fig. 6. Every β-lactam tested except flomox (cefcapene pivoxil hydrochloride) showed covalent attachment to the protein. These compounds were, in ascending order of molecular mass, faropenem (285 Da), imipenem (299 Da), penicillin-G (334 Da), cephalexin (347 Da), ampicillin (349 Da), oxacillin (401 Da), cefoxitin (427 Da), and cefotaxime (455 Da). Flomox is substantially larger than the other drugs tested, with a molecular mass of 622 Da, and its size apparently prevents it from interacting productively with SA-PBP3. As a negative control, the S392A mutant was also tested, but with the active-site serine residue missing this protein showed no attachment of any β-lactam. The mass spectrometry results show that the absence of ampicillin or cephalexin from the active site of the co-crystal structure cannot be ascribed to a lack of reactivity with the protein. Instead, it appears that SA-PBP3 is able to hydrolyze away the drug residue over the 12-h period of soaking. Cefotaxime is more resilient to removal from the active site, presumably in part because of its larger size blocking the close approach of water molecules to the active-site serine residue, but the structures offer no convincing explanation for the longevity of the cefotaxime acyl complex. The mass spectrometry shows a mass increase of 395 Da after reaction with cefotaxime, rather than the expected 455 Da, corroborating the loss of an acetoxy group suggested by the electron density.

Discussion

In this paper, we have sought to understand the structure of PBP3 from *S. aureus* and the nature of its interactions with substrates. Despite decades of research, PBP substrate specificity remains a topic of debate due to the recalcitrance of these enzymes to catalyze *in vitro* the reactions that they readily perform *in vivo*.[38] Overall among PBPs, ease of inhibition shows some correlation with the openness of the active site, although it has been widely found that mutations throughout a PBP structure may influence its reactivity. Our crystal structure shows that the active site of SA-PBP3 is not sterically occluded in the apo form, and the active-site serine is in a suitable position for reaction with sufficiently small β-lactams, consistent with its relative sensitivity to such compounds.[35] Cefotaxime, developed in 1979, is a third-generation cephalosporin. Compounds in this group are generally known for their broad spectrum activity against Gram-negative pathogens rather than Gram-positive pathogens and for their improved resistance to β-lactamases than earlier generations of β-lactams due to their 7β-(aminothiazoyl)oxyiminoacetamido side chain.[39] Cephalosporins developed specifically to tackle MRSA have a long hydrophobic 3′ side chain with a basic group at the end; this fits the narrow and rather negatively charged cleft into which it must fit to bind SA-PBP2a.[24,39]

Some PBPs show subsites in the substrate pocket that are thought to be involved in substrate specificity via recognition of the stem peptide, for example, the

Fig. 6. NanoESI mass spectrum of PBP3 (wild type and mutant Ala392) in the denatured state. The molecular masses of the ligand-bound forms were obtained by deconvolution of the original nanoESI mass spectra. (a) Samples of wild-type SA-PBP3 were dialyzed with a variety of antibiotics before denaturation and analysis. The measured mass of the apoprotein showed excellent agreement with the expected value of 72,234 Da (upper panel). Increases in mass were seen with every β-lactam examined except flomox. Only the results with cefotaxime and flomox are shown, in the middle and lower panels, with the chemical structure of each compound. Cefotaxime has a molecular mass of 455 Da but gave an observed mass increase of 395 Da, suggesting loss of the acetoxy group highlighted in red. (b) Mutant Ala392. Samples of the mutant were treated identically with the wild-type protein, but no increase in mass was observed with any compound.

class C low-molecular-weight PBPs *E. coli* PBP4,[40] *B. subtilis* PBP4a, *Actinomadura* R39 DD-peptidase,[41,42] and *E. coli* PBP5.[43,44] This hypothesis is supported by the recently solved X-ray crystal structure of *Actinomadura* R39 DD-peptidase in complex with a cephalosporin bearing a peptidoglycan mimetic side chain.[45] This model shows specific interactions between the ammonium carboxylate group of *meso*-2,6-diaminopimelic acid and a subsite composed of Asp142, Tyr147, Arg351, and Ser415 (*Actinomadura* R39 numbering). SA-PBP3 has no equivalent residues, and the space between residues 424–427 and 621–623 is comparatively wide.

Despite the presence of the so-called dimerization domain within the sequence and an apparently tight dimer interface formed by β-strands elsewhere in the N-domain, the protein shows no tendency to associate in solution. SA-PBP3 appears to be a cautionary example showing that bioinformatics tools alone are unreliable predictors of protein structure and association. The dimer interface revealed by the crystal structure may be relevant *in vivo*, possibly as part of a larger protein complex, with PBP3 attached to the cell membrane at its N-terminus. Since the N-terminal region of each subunit faces the same direction, attachment of each subunit to the membrane does not preclude dimer formation. The fact that PBP3 deletion mutants grow better than wild-type *S. aureus* under conditions where PBP3 is inhibited suggests that the protein associates into a heterocomplex that operates better without PBP3 than with inactive PBP3.[12] The nature of such a complex is presently unclear.

Materials and Methods

Cloning, expression, and purification of PBP3

The PBP3 gene was amplified by PCR using cloned cDNA (*S. aureus*/MW2) obtained from the National Institute of Technology and Evaluation. The primers used were 5′-GGGCCCGGATCCCAAGGCTCACATTATAAACAAATTATAAA-3′ and 5′-GGGCCCGCGGCCGCCGCGCGTTATTTGTCTTTGTCTTTATTT-3′.

The product, encoding PBP3 residues 46–691, was digested with BamHI and NotI and then ligated into suitably cut modified pET28b vector, in which a Shine–Dalgarno sequence, an initial ATG, a hexa-histidine tag, and a tobacco etch virus (TEV) protease cleavage site had been cloned between XbaI and BamHI restriction sites. The pET28b/PBP3 plasmid was transformed into *E. coli* BL21(DE3). Cells were grown at 37 °C in LB medium containing 50 μg/ml kanamycin up to OD_{600} between 0.6 and 0.8. Protein expression was induced by adding IPTG to a final concentration of 0.5 mM and incubating the culture with shaking at 15 °C overnight. After harvesting by centrifugation at 4000*g* for 15 min, we resuspended cells in Ni-NTA binding buffer [20 mM Tris (pH 8.0), 500 mM NaCl, 500 mM urea, 25 mM imidazole, and 10 mM 2-mercaptoethanol] and lysed by sonication. After centrifugation at 40,000*g* for 30 min, the supernatant was loaded onto a 20-ml Ni-NTA Sepharose column (QIAGEN) equilibrated with the same buffer. Protein was eluted by a 25- to 500-mM linear gradient of imidazole. Peak fractions were collected, and His tag was removed with 0.2 μM His-tagged TEV protease at room temperature while dialyzing for overnight against Ni-NTA binding buffer. The molar ratio of PBP3 to TEV protease was 10:1. Protein was reloaded onto the same Ni-NTA Sepharose column to remove His-tagged protein, including TEV protease, and minor protein contaminants. The fractions containing PBP3 were dialyzed against SP binding buffer [20 mM sodium phosphate (pH 6.0) and 100 mM NaCl] and were loaded onto SP-Sepharose (GE Healthcare) equilibrated with the same buffer. Protein was eluted using a linear gradient of 100–1000 mM NaCl. The peak fractions were directly loaded onto a hydroxyapatite column (Bio-Rad) and eluted with a 20- to 1000-mM linear gradient of potassium phosphate (pH 6.0). Finally, protein was dialyzed overnight against crystallization buffer [20 mM Tris–HCl (pH 8.0) and 100 mM NaCl] and passed through Q-Sepharose (GE Healthcare) to separate off minor protein and nucleic acid contaminants. The sample was concentrated to 20 mg/ml by ultrafiltration using a Centriprep YM-30 (Millipore).

Mutagenesis

Site-directed mutagenesis replacing Ser392 to alanine was carried out with a simple PCR procedure. The regions encoding residues 46–392 and 392–691 were amplified using the following pairs of forward and reverse primers, respectively:

5′-GGGCCCGGATCCCAAGGCTCACATTATAAACAAATTATAAA-3′ with 5′-GCTAATAATGTTCCACCTTTTACAGAAGCTCCAACCGCAAATTGAGAAGTAAACGTACC-3′ for the N-terminal region and 5′-GGTACGTTTACTTCTCAATTTGCGGTTGGAGCTTCTGTAAAAGGTGGAACATTATTAGC-3′ with 5′-GGGCCCGCGGCCGCCGCGCGTTATTTGTCTTTGTCTTTATTT-3′ for the C-terminal region. The reverse primer for the N-terminal region is the reverse complement of the forward primer for the C-terminal region. The purified overlapping fragments were joined together and amplified by PCR and then treated with BamHI and NotI. The fragment was ligated into suitably cut modified pET28b vector. Mutant protein was expressed and purified using the same protocol as for the wild type.

Crystallization

PBP3 was crystallized by the vapor diffusion hanging-drop method. Drops were formed by mixing 1.5 μl of protein solution with 1.5 μl of reservoir solution, then equilibrated against 500 μl of reservoir solution at 20 °C. Crystals of native and Se-Met PBP3 were grown in 2.0 M AmSO4, 0.5 M LiCl, and 5% (v/v) glycerol and 1.8 M AmSO4 and 0.4 M $NaNO_3$, respectively. For heavy-atom derivatization, crystals were soaked in reservoir solution containing 0.5 mM thimerosal (Hg) or 0.5 mM K_2PtCl_4 for 12 h before data collection. Crystals formed in the space

Table 1. Statistics of the crystallographic analysis

	Native	Cefotaxime	Se-Met	Hg	Pt
Data sets					
Space group	$P4_32_12$				
Unit cell					
a, *b*, *c* (Å)	143.4, 143.4, 189.4	143.0, 143.0, 189.6	143.4, 143.4, 189.6	142.8, 142.8, 190.6	142.4, 142.4, 190.4
Resolution range (Å)	50.0–2.3	50.0–2.4	20.0–2.9	50.0–3.2	50.0–3.3
Reflections (measured/unique)	483,661/85,132	431,478/76,011	845,441/43,698	484,063/33,363	427,946/30,123
Completeness (overall/outer shell, %)[a]	96.7/89.4	98.2/89.0	97.8/80.0	100/100	100/99.0
R_{merge} (overall/outer shell, %)[a]	9.0/49.4	11.1/46.0	11.7/39.5	10.5/51.5	10.2/56.1
Redundancy (overall/outer shell)	5.7/3.0	5.7/2.3	19.3/4.0	14.5/14.8	14.2/14.5
Mean $\langle I/\sigma(I)\rangle$ (overall/outer shell)	15.9/1.5	11.4/1.4	24.2/1.8	38.1/7.6	45.9/7.4
Overall *B*-factor from Wilson plot (Å^2)	35.0	31.8	62.2	84.2	98.0
Metal sites			19	5	10
Phasing (20.0–2.3 Å)					
Mean FOM[b] after SHARP phasing (acentric/centric)			0.831/0.767	0.369/0.377	0.230/0.270
Refinement statistics					
Resolution range (Å)	50.0–2.3	50.0–2.4			
R-factor[c]/R_{free} (%)[c]	26.0/30.0	25.2/31.0			
rmsd bond lengths (Å)/bond angles (°)	0.010/1.461	0.010/1.465			
Number of water molecules	260	306			
Average *B*-factor (PBP3/water/ligand, Å^2)	77/51	69/45/103			
Ramachandran plot (%)					
Residues in most favorable regions	82.0	81.3			
Residues in additional allowed regions	16.9	17.4			
Residues in generously allowed regions	1.1	1.3			
Residues in disallowed regions	0	0			

The highest-resolution shells from left to right are 2.38–2.30, 2.44–2.40, 3.00–2.90, 3.31–3.20, and 3.42–3.30 Å, respectively.

[a] Completeness and R_{merge} are given for the overall data and for the highest-resolution shell.

[b] Figure of merit (FOM)= $|F\text{best}| - |F|$.

[c] $R_{merge}=\sum|I_i-\langle I\rangle|/\sum|I_i|$, where I_i is the intensity of an observation and $\langle I\rangle$ is the intensity in the mean value for that reflection, and the summations are over all equivalents. *R*-factor=$\sum h||F_o(h)|-|F_c(h)||/\sum hF_o(h)$, where F_o and F_c are the observed and calculated structure factor amplitudes, respectively. R_{free} was calculated with 5% of the data excluded from the refinement.

group $P4_32_12$, with $a=b=143.4$ Å and $c=189.3$ Å and contained two molecules per asymmetric unit. Diffraction data were collected at −180 °C using crystals flash-frozen in crystallization buffer containing 17.5% (v/v) glycerol and 2.5% (v/v) dimethyl sulfoxide. Diffraction data from a native crystal were collected at 0.9 Å on beamline BL44XU stations at the SPring8, Harima, Japan, using a MX225HE detector. Derivative data were collected at 0.97909 Å (for Se-Met) and 1.0 Å (for Hg and Pt) on beamline BL17A stations at the Photon Factory, Tsukuba, Japan, using an ADSC Quantum 315 CCD detector. Crystals of the antibiotic complex were prepared by dissolving cefotaxime sodium salt (Wako) in the reservoir solution to 5 mM concentration and then adding 0.4 µl of this solution directly to the hanging drops containing protein crystals. Soaking was carried out for 12 h at 20 °C. Diffraction data were collected at 1.0 Å on beamline PF-BL1A at the Photon Factory. All data were processed and scaled using HKL2000 and scaled with SCALEPACK.[46]

Structure determination and refinement

The native and derivative data sets were used for phasing by MIR (*m*ultiple *i*somorphous *r*eplacement) using SHELXD[47] and Auto-SHARP.[48] Se-Met, platinum, and mercury sites and initial phases were determined using SHELXD. Solvent flattening using SOLOMON[49] in Auto-SHARP was used to improve phases. After density modification, an electron density map was calculated to a resolution of 2.3 Å. The map was of good quality, allowing much of the main chain to be traced. Successive rounds of model building were carried out using Coot[50]; refinement, using both REFMAC5[51] and PHENIX.[25] After an initial round of simulated annealing refinement, several macrocycles that included bulk solvent correction and anisotropic scaling of the data, individual coordinate refinement with minimization, and individual isotropic atomic displacement parameter refinement were carried out with maximum likelihood as the target. Non-crystallographic symmetry restraints were not applied. In the course of the refinement, water molecules were added to the models by manual inspection of their positions in both $2F_o-F_c$ and F_o-F_c maps, and combined TLS (*T*ranslation/*L*ibration/*S*crew) and individual atomic displacement parameter refinement were carried out in the final stages. The stereochemistry of the final model was assessed using Coot. Data collection and refinement statistics are shown in Table 1.

Analytical ultracentrifugation

The molecular weight and self-association of PBP3 in solution were examined using a Beckman Optima XL-1 analytical ultracentrifuge. The experiments were performed

at 20 °C, and absorbance at 280 nm was measured. Before the experiment, the sample was diluted to 10 μM with crystallization buffer. After thermal equilibration at rest for 2 h, sedimentation velocity data were measured at 50,000 rpm for 6 h and analyzed using SEDFIT version 9.4.[52]

NanoESI mass spectrometry

Nanoelectrospray ionization (nanoESI) mass spectra of free and ligand-bound PBP3 were obtained by Q-Tof-2 (Waters, Milford, MA) with a nanoelectrospray ion source. To observe the native state of free PBP3 in solution, we prepared the PBP3 samples by dialysis against 100 mM ammonium acetate. The final concentration of PBP3 was estimated to be ~20 μM. PBP3 wild type and S392A mutant were mixed with antibiotic at a 1:1 molar ratio, dialyzed against 5 mM ammonium acetate, and diluted with 0.1% formic acid in 50% acetonitrile to make the final concentration to be ~10 μM in order to determine the masses of the ligand-bound forms more accurately.

An aliquot of 4 μl of each sample solution was placed in a HUMANIX nanoESI tip (Hiroshima, Japan) and electrosprayed with an applied capillary voltage of 1.0 kV. The pressure in the quadrupole ion guide of Q-Tof-2 was controlled by throttling down the Speedivalve fitted to the rotary pump if necessary. Each mass spectrum was acquired in 4 s, and more than 10 spectra were accumulated and smoothed with the Savitzky–Golay method. The program MaxEnt3 was used to deconvolute the original nanoESI mass spectra and determine the molecular masses of the ligand-bound forms.

Accession numbers

The models have been deposited in the Research Collaboratory for Structural Bioinformatics Protein Data Bank (PDB) with accession codes 3VSK (apo PBP3) and 3VSL (PBP3 with cefotaxime).

Acknowledgements

We thank staff at beamlines BL44XU and BL1A at SPring8 and the Photon Factory for assistance with data collection. S.-Y.P. is supported in part by the ISS Applied Research Partnership Program, Maura Foods and Biosciences Inc., and Confocal Science Inc. This work was supported in part by the Medical Research Council grants G0400848 and G500643 to D.I.R. and grants-in-aid from the Ministry of Education, Culture, Sports, Science and Technology of Japan to J.R.H.T.

References

1. Vollmer, W., Blanot, D. & de Pedro, M. A. (2008). Peptidoglycan structure and architecture. *FEMS Microbiol. Rev.* **32**, 149–167.
2. Sauvage, E., Kerff, F., Terrak, M., Ayala, J. A. & Charlier, P. (2008). The penicillin-binding proteins: structure and role in peptidoglycan biosynthesis. *FEMS Microbiol. Rev.* **32**, 234–258.
3. Ubukata, K., Nonoguchi, R., Matsuhashi, M. & Konno, M. (1989). Expression and inducibility in *Staphylococcus aureus* of the *mecA* gene, which encodes a methicillin-resistant *S. aureus*-specific penicillin-binding protein. *J. Bacteriol.* **171**, 2882–2885.
4. Morell, E. A. & Balkin, D. M. (2010). Methicillin-resistant *Staphylococcus aureus*: a pervasive pathogen highlights the need for new antimicrobial development. *Yale J. Biol. Med.* **83**, 223–233.
5. Banerjee, R., Gretes, M., Harlem, C., Basuino, L. & Chambers, H. F. (2010). A *mecA*-negative strain of methicillin-resistant *Staphylococcus aureus* with high-level β-lactam resistance contains mutations in three genes. *Antimicrob. Agents Chemother.* **54**, 4900–4902.
6. Tipper, D. J. & Strominger, J. L. (1965). Mechanism of action of penicillins: a proposal based on their structural similarity to acyl-D-alanyl-D-alanine. *Proc. Natl Acad. Sci. USA*, **54**, 1133–1141.
7. Contreras-Martel, C., Dahout-Gonzalez, C., Martins Ados, S., Kotnik, M. & Dessen, A. (2009). PBP active site flexibility as the key mechanism for β-lactam resistance in pneumococci. *J. Mol. Biol.* **387**, 899–909.
8. Goffin, C. & Ghuysen, J. M. (1998). Multimodular penicillin-binding proteins: an enigmatic family of orthologs and paralogs. *Microbiol. Mol. Biol. Rev.* **62**, 1079–1093.
9. Ghosh, A. S., Chowdhury, C. & Nelson, D. E. (2008). Physiological functions of D-alanine carboxypeptidases in *Escherichia coli*. *Trends Microbiol.* **16**, 309–317.
10. Memmi, G., Filipe, S. R., Pinho, M. G., Fu, Z. & Cheung, A. (2008). *Staphylococcus aureus* PBP4 is essential for β-lactam resistance in community-acquired methicillin-resistant strains. *Antimicrob. Agents Chemother.* **52**, 3955–3966.
11. Navratna, V., Nadig, S., Sood, V., Prasad, K., Arakere, G. & Gopal, B. (2010). Molecular basis for the role of *Staphylococcus aureus* penicillin binding protein 4 in antimicrobial resistance. *J. Bacteriol.* **192**, 134–144.
12. Pinho, M. G., de Lencastre, H. & Tomasz, A. (2000). Cloning, characterization, and inactivation of the gene *pbpC*, encoding penicillin-binding protein 3 of *Staphylococcus aureus*. *J. Bacteriol.* **182**, 1074–1079.
13. Fraipont, C., Alexeeva, S., Wolf, B., van der Ploeg, R., Schloesser, M., den Blaauwen, T. & Nguyen-Disteche, M. (2011). The integral membrane FtsW protein and peptidoglycan synthase PBP3 form a subcomplex in *Escherichia coli*. *Microbiology*, **157**, 251–259.
14. Piette, A., Fraipont, C., Den Blaauwen, T., Aarsman, M. E., Pastoret, S. & Nguyen-Disteche, M. (2004). Structural determinants required to target penicillin-binding protein 3 to the septum of *Escherichia coli*. *J. Bacteriol.* **186**, 6110–6117.
15. Nguyen-Disteche, M., Fraipont, C., Buddelmeijer, N. & Nanninga, N. (1998). The structure and function of *Escherichia coli* penicillin-binding protein 3. *Cell. Mol. Life Sci.* **54**, 309–316.
16. Georgopapadakou, N. H., Dix, B. A. & Mauriz, Y. R. (1986). Possible physiological functions of penicllin-binding proteins in *Staphylococcus aureus*. *Antimicrob. Agents Chemother.* **29**, 333–336.

17. Sung, M. T., Lai, Y. T., Huang, C. Y., Chou, L. Y., Shih, H. W., Cheng, W. C. *et al.* (2009). Crystal structure of the membrane-bound bifunctional transglycosylase PBP1b from *Escherichia coli*. *Proc. Natl Acad. Sci. USA*, **106**, 8824–8829.
18. Powell, A. J., Tomberg, J., Deacon, A. M., Nicholas, R. A. & Davies, C. (2009). Crystal structures of penicillin-binding protein 2 from penicillin-susceptible and -resistant strains of *Neisseria gonorrhoeae* reveal an unexpectedly subtle mechanism for antibiotic resistance. *J. Biol. Chem.* **284**, 1202–1212.
19. Sainsbury, S., Bird, L., Rao, V., Shepherd, S. M., Stuart, D. I., Hunter, W. N. *et al.* (2011). Crystal structures of penicillin-binding protein 3 from *Pseudomonas aeruginosa*: comparison of native and antibiotic-bound forms. *J. Mol. Biol.* **405**, 173–184.
20. Han, S., Zaniewski, R. P., Marr, E. S., Lacey, B. M., Tomaras, A. P., Evdokimov, A. *et al.* (2010). Structural basis for effectiveness of siderophore-conjugated monocarbams against clinically relevant strains of *Pseudomonas aeruginosa*. *Proc. Natl Acad. Sci. USA*, **107**, 22002–22007.
21. Contreras-Martel, C., Job, V., Di Guilmi, A. M., Vernet, T., Dideberg, O. & Dessen, A. (2006). Crystal structure of penicillin-binding protein 1a (PBP1a) reveals a mutational hotspot implicated in β-lactam resistance in *Streptococcus pneumoniae*. *J. Mol. Biol.* **355**, 684–696.
22. Pares, S., Mouz, N., Petillot, Y., Hakenbeck, R. & Dideberg, O. (1996). X-ray structure of *Streptococcus pneumoniae* PBP2x, a primary penicillin target enzyme. *Nat. Struct. Biol.* **3**, 284–289.
23. Lovering, A. L., de Castro, L. H., Lim, D. & Strynadka, N. C. (2007). Structural insight into the transglycosylation step of bacterial cell-wall biosynthesis. *Science*, **315**, 1402–1405.
24. Lim, D. & Strynadka, N. C. (2002). Structural basis for the β lactam resistance of PBP2a from methicillin-resistant *Staphylococcus aureus*. *Nat. Struct. Biol.* **9**, 870–876.
25. Adams, P. D., Afonine, P. V., Bunkoczi, G., Chen, V. B., Davis, I. W., Echols, N. *et al.* (2010). PHENIX: a comprehensive Python-based system for macromolecular structure solution. *Acta Crystallogr., Sect. D: Biol. Crystallogr.* **66**, 213–221.
26. Gouet, P., Courcelle, E., Stuart, D. I. & Metoz, F. (1999). ESPript: multiple sequence alignments in PostScript. *Bioinformatics*, **15**, 305–308.
27. Lovering, A. L., De Castro, L. & Strynadka, N. C. (2008). Identification of dynamic structural motifs involved in peptidoglycan glycosyltransfer. *J. Mol. Biol.* **383**, 167–177.
28. Goffin, C., Fraipont, C., Ayala, J., Terrak, M., Nguyen-Disteche, M. & Ghuysen, J. M. (1996). The non-penicillin-binding module of the tripartite penicillin-binding protein 3 of *Escherichia coli* is required for folding and/or stability of the penicillin-binding module and the membrane-anchoring module confers cell septation activity on the folded structure. *J. Bacteriol.* **178**, 5402–5409.
29. Punta, M., Coggill, P. C., Eberhardt, R. Y., Mistry, J., Tate, J., Boursnell, C. *et al.* (2012). The Pfam protein families database. *Nucleic Acids Res.* **40**, D290–D301.
30. Krissinel, E. & Henrick, K. (2004). Secondary-structure matching (SSM), a new tool for fast protein structure alignment in three dimensions. *Acta Crystallogr., Sect. D: Biol. Crystallogr.* **60**, 2256–2268.
31. Krissinel, E. & Henrick, K. (2007). Inference of macromolecular assemblies from crystalline state. *J. Mol. Biol.* **372**, 774–797.
32. Tame, J. R. H. (1999). Scoring functions: a view from the bench. *J. Comput.-Aided Mol. Des.* **13**, 99–108.
33. Tame, J. R. H. (2005). Scoring functions—the first 100 years. *J. Comput.-Aided Mol. Des.* **19**, 445–451.
34. Kishida, H., Unzai, S., Roper, D. I., Lloyd, A., Park, S. Y. & Tame, J. R. H. (2006). Crystal structure of penicillin binding protein 4 (dacB) from *Escherichia coli*, both in the native form and covalently linked to various antibiotics. *Biochemistry*, **45**, 783–792.
35. Georgopapadakou, N. H., Smith, S. A. & Bonner, D. P. (1982). Penicillin-binding proteins in a *Staphylococcus aureus* strain resistant to specific β-lactam antibiotics. *Antimicrob. Agents Chemother.* **22**, 172–175.
36. Contreras-Martel, C., Amoroso, A., Woon, E. C., Zervosen, A., Inglis, S., Martins, A. *et al.* (2011). Structure-guided design of cell wall biosynthesis inhibitors that overcome β-lactam resistance in *Staphylococcus aureus* (MRSA). *ACS Chem. Biol.* **6**, 943–951.
37. Tomberg, J., Unemo, M., Davies, C. & Nicholas, R. A. (2010). Molecular and structural analysis of mosaic variants of penicillin-binding protein 2 conferring decreased susceptibility to expanded-spectrum cephalosporins in *Neisseria gonorrhoeae*: role of epistatic mutations. *Biochemistry*, **49**, 8062–8070.
38. Josephine, H. R., Charlier, P., Davies, C., Nicholas, R. A. & Pratt, R. F. (2006). Reactivity of penicillin-binding proteins with peptidoglycan-mimetic β-lactams: what's wrong with these enzymes? *Biochemistry*, **45**, 15873–15883.
39. Page, M. G. P. (2012). Beta-lactam antibiotics. In *Antibiotic Discovery and Development* (Dougherty, T. J. & Pucci, M. J., eds), Springer, Berlin, Germany.
40. Clarke, T. B., Kawai, F., Park, S. Y., Tame, J. R. H., Dowson, C. G. & Roper, D. I. (2009). Mutational analysis of the substrate specificity of *Escherichia coli* penicillin binding protein 4. *Biochemistry*, **48**, 2675–2683.
41. Pratt, R. F. (2008). Substrate specificity of bacterial DD-peptidases (penicillin-binding proteins). *Cell. Mol. Life Sci.* **65**, 2138–2155.
42. Sauvage, E., Herman, R., Petrella, S., Duez, C., Bouillenne, F., Frere, J. M. & Charlier, P. (2005). Crystal structure of the *Actinomadura* R39 DD-peptidase reveals new domains in penicillin-binding proteins. *J. Biol. Chem.* **29**, 29.
43. Nicholas, R. A., Krings, S., Tomberg, J., Nicola, G. & Davies, C. (2003). Crystal structure of wild-type penicillin-binding protein 5 from *Escherichia coli*: implications for deacylation of the acyl-enzyme complex. *J. Biol. Chem.* **278**, 52826–52833.
44. Nicola, G., Tomberg, J., Pratt, R. F., Nicholas, R. A. & Davies, C. (2010). Crystal structures of covalent complexes of β-lactam antibiotics with *Escherichia coli* penicillin-binding protein 5: toward an understanding of antibiotic specificity. *Biochemistry*, **49**, 8094–8104.

45. Sauvage, E., Powell, A. J., Heilemann, J., Josephine, H. R., Charlier, P., Davies, C. & Pratt, R. F. (2008). Crystal structures of complexes of bacterial DD-peptidases with peptidoglycan-mimetic ligands: the substrate specificity puzzle. *J. Mol. Biol.* **381**, 383–393.
46. Otwinowski, Z. & Minor, W. (1997). Processing of X-ray diffraction data collected in oscillation mode. *Methods Enzymol.* **276**, 307–326.
47. Schneider, T. R. & Sheldrick, G. M. (2002). Substructure solution with SHELXD. *Acta Crystallogr., Sect. D: Biol. Crystallogr.* **58**, 1772–1779.
48. Vonrhein, C., Blanc, E., Roversi, P. & Bricogne, G. (2007). Automated structure solution with autoSHARP. *Methods Mol. Biol.* **364**, 215–230.
49. Abrahams, J.-P. & Leslie, A. G. W. (1996). Methods used in the structure determination of bovine mitochondrial F1 ATPase. *Acta Crystallogr., Sect. D: Biol. Crystallogr.* **52**, 30–42.
50. Emsley, P., Lohkamp, B., Scott, W. G. & Cowtan, K. (2010). Features and development of Coot. *Acta Crystallogr., Sect. D: Biol. Crystallogr.* **66**, 486–501.
51. Murshudov, G. N., Vagin, A. A. & Dodson, E. J. (1997). Refinement of macromolecular structures by the maximum-likelihood method. *Acta Crystallogr., Sect. D: Biol. Crystallogr.* **53**, 240–255.
52. Brown, P. H. & Schuck, P. (2008). A new adaptive grid-size algorithm for the simulation of sedimentation velocity profiles in analytical ultracentrifugation. *Comput. Phys. Commun.* **178**, 105–120.

JVI
Journals.ASM.org

Structural Basis for Broad Detection of Genogroup II Noroviruses by a Monoclonal Antibody That Binds to a Site Occluded in the Viral Particle

Grant S. Hansman,[a,b] David W. Taylor,[c,d] Jason S. McLellan,[b] Thomas J. Smith,[e] Ivelin Georgiev,[b] Jeremy R. H. Tame,[f] Sam-Yong Park,[f] Makoto Yamazaki,[g] Fumio Gondaira,[g] Motohiro Miki,[a,g] Kazuhiko Katayama,[a] Kazuyoshi Murata,[d] and Peter D. Kwong[b]

Department of Virology II, National Institute of Infectious Diseases, Tokyo, Japan[a]; Vaccine Research Center, National Institute of Allergy and Infectious Diseases, National Institutes of Health, Bethesda, Maryland, USA[b]; Department of Molecular Biophysics and Biochemistry, Yale University School of Medicine, New Haven, Connecticut, USA[c]; National Institute for Physiological Sciences, Okazaki, Japan[d]; Donald Danforth Plant Science Center, Saint Louis, Missouri, USA[e]; Protein Design Laboratory, Yokohama City University, Yokohama, Japan[f]; and Denka-Seiken Co. Ltd., Niigata, Japan[g]

Human noroviruses are genetically and antigenically highly divergent. Monoclonal antibodies raised in mice against one kind of norovirus virus-like particle (VLP), however, were found to have broad recognition. In this study, we present the crystal structure of the antigen-binding fragment (Fab) for one of these broadly reactive monoclonal antibodies, 5B18, in complex with the capsid-protruding domain from a genogroup II genotype 10 (GII.10) norovirus at 3.3-Å resolution and, also, the cryo-electron microscopy structure of the GII.10 VLP at ~10-Å resolution. The GII.10 VLP structure was more similar in overall architecture to the GV.1 murine norovirus virion than to the prototype GI.1 human norovirus VLP, with the GII.10 protruding domain raised ~15 Å off the shell domain and rotated ~40° relative to the GI.1 protruding domain. In the crystal structure, the 5B18 Fab bound to a highly conserved region of the protruding domain. Based on the VLP structure, this region is involved in interactions with other regions of the capsid and is buried in the virus particle. Despite the occluded nature of the recognized epitope in the VLP structure, enzyme-linked immunosorbent assay (ELISA) binding suggested that the 5B18 antibody was able to capture intact VLPs. Together, the results provide evidence that the norovirus particle is capable of extreme conformational flexibility, which may allow for antibody recognition of conserved surfaces that would otherwise be buried on intact particles.

The family *Caliciviridae* contains four genera, *Norovirus*, *Sapovirus*, *Lagovirus*, and *Vesivirus*, which include norovirus, sapovirus, rabbit hemorrhagic disease virus, and feline calicivirus strains, respectively. Human noroviruses are the dominant cause of outbreaks of gastroenteritis and are genetically and antigenically distinct (21). Two main genogroups (GI and -II) of human noroviruses are mostly responsible for causing human infections, and these two genogroups are further subdivided into numerous genotypes (GI.1 to -8 and GII.1 to -17) (72). The human norovirus genome has three open reading frames (ORF1 to -3), where ORF1 encodes the nonstructural proteins, ORF2 encodes the capsid protein, and ORF3 encodes a small structural protein. Human noroviruses cannot be grown in cell culture, but the expression of the capsid protein in a baculovirus expression system leads to the self-assembly of nucleic acid-free virus-like particles (VLPs) that are believed to be morphologically and antigenically similar to the native virion (27).

The cryo-electron microscopy (cryo-EM) and X-ray crystal structures of the prototype norovirus VLP (GI.1, Norwalk virus) show that the VLP form a T=3 icosahedral structure (53, 54). The VLP can be divided into two domains, the shell (S) and the protruding (P) domains. The S domain forms a scaffold surrounding the RNA, whereas the P domain, which is further subdivided into P1 and P2 subdomains, is thought to contain the determinants of cell attachment and strain diversity (27, 53, 60). The P domain forms 90 dimer subunits, termed A/B and C/C. Interestingly, the P domains alone can be expressed in *Escherichia coli*, and these form P domain dimers that are biologically relevant (60). The X-ray crystal structures of several human norovirus P domains (GI.1, GII.4, GII.10, and GII.12) indicate that their overall structures are similar and resemble the P domain on the VLPs, with a single α-helix in the P1 subdomain and six antiparallel β-strands in the P2 subdomain (7, 10, 13, 22). The X-ray crystal structure of a GV.1 murine norovirus P domain reveals a structure that is similar overall to the human norovirus P domains (63). However, cryo-electron microscopy (cryo-EM) studies show that in the GV.1 murine norovirus virion, the P domain is raised off the S domain by ~16 Å (30), while in the GI.1 and GII.4 (Grimsby virus strain) human norovirus VLPs, the P domain rests directly on the S domain (12, 53, 54). In addition, the GV.1 murine norovirus P domain is rotated 40° clockwise with respect to the GI.1 and GII.4 human norovirus P domains.

Human noroviruses are generally detected using reverse transcription-PCR (RT-PCR) with degenerate primers or enzyme-linked immunosorbent assay (ELISA) with norovirus-specific antibodies. Many of the polyclonal and monoclonal antibodies (MAbs) used in the ELISA kits were developed in mice immunized with norovirus VLPs (15, 28, 55, 57), and most have broad recognition (21, 39, 40, 50, 59, 70). Several antibodies are found to bind to the S domain (39, 70), while others bound to the P domain (50, 59). However,

Received 23 November 2011 **Accepted** 10 January 2012
Published ahead of print 25 January 2012
Address correspondence to Peter D. Kwong, pdkwong@nih.gov, or Kazuyoshi Murata, kazum@nips.ac.jp.
Supplemental material for this article may be found at http://jvi.asm.org/.

doi:10.1128/JVI.06868-11